Final Scientific/Technical Report **WRI/EP&G-17-001**

Sorbent-based Oxygen Production for Energy Systems

Cooperative Agreement DE-FE0024075

October 1, 2014 to September 30, 2016

For
U.S. Department of Energy
Office of Fossil Energy
National Energy Technology Laboratory
Morgantown, West Virginia

By
Dr. Vijay K. Sethi
Sr. Vice President
Western Research Institute
3474 North 3rd Street
Laramie, Wyoming 82072
vsethi@uwyo.edu
307-721-2376

Project Participants:
Dr. Jerry Lin, Arizona State University
Dr. Shuguang Deng, Arizona State University
Dr. Matthew Targett, LP Amina

January 31, 2017

Signature of Submitting Official: Vijay Sethi

Digitally signed by Vijay Sethi
DN: cn=Vijay Sethi, o=Western Research Institute, ou=Energy Production and Generation, email=vsethi@uwyo.edu, c=US
Date: 2017.04.21 15:02:02 -06'00'

Dr. Vijay K. Sethi, PI/PD

DISCLAIMER

TABLE OF CONTENTS

LIST OF TABLES AND FIGURES

Table **Page**

Figure **Page**

LIST OF TABLES AND FIGURES (Continued)

Figure **Page**

.

ABSTRACT

Project DE-FE0024075 deals with the development of a moderate-temperature sorbent-based oxygen production technology. Sorbent-based oxygen production process utilizes oxygen-storage properties of Perovskites to (1) adsorb oxygen from air in a solid sorbent, and (2) release the adsorbed oxygen into a sweep gas such as CO_2 and/or steam for gasification systems or recycled flue gas for oxy-combustion systems. Pure oxygen can be produced by the use of vacuum instead of a sweep gas to affect the pressure swing.

By developing more efficient and stable, higher sorption capacity, newer class of materials operating at moderate temperatures this process represents a major advancement in air separation technology. Newly developed perovskite ceramic sorbent materials with order-disorder transition have a higher O_2 adsorption capacity, potentially 200 ºC lower operating temperatures, and up to two orders of magnitude faster desorption rates than those used in earlier development efforts. The performance advancements afforded by the new materials lead to substantial savings in capital investment and operational costs. Cost of producing oxygen using sorbents could be as much as 26% lower than VPSA and about 13% lower than a large cryogenic air separation unit. Cost advantage against large cryogenic separation is limited because sorbent-based separation numbers up sorbent modules for achieving the larger capacity.

EXECUTIVE SUMMARY

Development of a sorbent-based oxygen production technology was undertaken. The sorbent-based oxygen production process utilizes oxygen-storage properties of Perovskites to (1) adsorb oxygen from air in a solid sorbent, and (2) release the adsorbed oxygen into a sweep gas such as CO_2 and/or steam for gasification systems or recycled flue gas for oxy-combustion systems. The process operation is made continuous by operating two or more fixed beds in a cyclic process, or through the use of moving beds. By developing more efficient and stable, higher sorption capacity, newer class of materials operating at moderate temperatures this process represents a major advancement in air separation technology. Cost of producing oxygen using sorbents could be as much as 26% lower than VPSA and about 13% lower than a large cryogenic air separation unit. Cost advantage against large cryogenic separation is limited because sorbent-based separation achieves the scale-up by numbering up the sorbent modules.

Newly developed perovskite ceramic sorbent materials with order-disorder transition have a higher O_2 adsorption capacity, potentially 200 ºC lower operating temperatures, and up to two orders of magnitude faster desorption rates than those used in earlier CAR process development efforts at Western Research Institute (WRI). The performance advancements lead to substantial savings in capital investment and operational costs. Furthermore, new mixed-conducting metal oxide ceramic sorbents with improved chemical stability address major short-coming of the classic sorbents used in earlier work.

Working with technology end-users, LP Amina, Inc., WRI assembled a team of researchers to develop the new sorbent materials and a continuous oxygen production process. The objectives of the proposed project were to: (i) develop and characterize an improved sorbent based on mixed-conducting metal oxide ceramic materials (ii) design and build a bench-scale continuous process to test the robustness of the materials, (iii) evaluate sorbent performance as a function of operational parameters.

Materials development work performed at Arizona State demonstrated that LSCF perovskite oxides exhibit fast oxygen sorption rate and good oxygen adsorption capacity. Gravimetric experimental results showed that the perovskite materials with disorder-to-order phase transition exhibit an oxygen desorption rate significantly faster than the materials without disorder-order phase transition. However, the disorder-order enhanced desorption rate is not observed in the fixed-bed desorption process. The oxygen partial pressure surrounding the sorbents is found to significantly affect the phase transition property. The oxygen partial pressure during the fixed-bed desorption process is above the equilibrium pressure of the ordered phase. Thus the phase transition only happens in the late stage of desorption during the fixed-bed oxygen desorption process. Study was conducted on other sorbent materials with improved separation capacity and chemical stability. The calcium-based sorbents are proven to be stable under CO_2 atmosphere at

800°C. Doping lanthanum and bismuth decreases the stability of the materials in CO_2 environment. However with strontium doping, desorption rate is significantly improved.

Sorbent performance was evaluated in a bench-scale setup with Helium, CO_2 and nitrogen sweep gases as well as with vacuum pressure swing. Several batches of sorbents were prepared in the form of pellets. Two different chemistries were used. Testing with LSCF 1991 and LSCF 2864 confirmed that indeed air-separation can be affected at temperatures as low as 550°C.

In the new class of materials, the order-to-disorder transition is an endothermic process, in contrast to the exothermic oxygen sorption process. By taking advantage of the synergistic heat effects of sorption/desorption and vacancy order/disorder, it is possible to design a nearly isothermal process with very low "apparent" heats of adsorption. The process can thereby operate at moderate temperatures yet has nearly hundred times faster desorption rates. Testing data also confirm the superior performance of the sorbent capacity for oxygen production.

Under vacuum pressure swing conditions, the bench-scale testing revealed the need for a rinse cycle to produce better than 95% pure oxygen. Based on testing concluded adsorption/desorption cycle proposed includes: quick pressurization, air flow at pressure, partial depressurization as a rinse and vacuum desorption to produce >95% pure oxygen.

LP Amina analysis of oxygen separation process based on new sorbents was found to offer the potential of significantly lower OPEX and somewhat lower CAPEX than the cryogenic alternative. The dual fixed bed adsorption setup can exploit a simpler layout with a lower parts count than a cryogenic oxygen plant, and thereby represents a smaller capital expenditure. Micro-channel and tube/shell-based heat exchanger designs offer significant promise and the potential for further lowering of the costs. Operating expenditures for the process are highly dependent on process efficiency assumptions, particularly relating to fuel consumption, heat loss, and perovskite properties. Based on the laboratory-scale data, the sorbent-based separation process outperforms cryogenic oxygen from an OPEX standpoint.

Sorbent-based Oxygen Production for Energy Systems

1. Introduction

Sorbent-based oxygen production process (Figure 1) utilizes oxygen-storage properties of perovskites to adsorb oxygen from air in a solid sorbent, and then releases the adsorbed oxygen into low oxygen partial pressure environment such as vacuum or a sweep gas such as CO_2 and/or steam. Oxygen is stored in the oxide lattice during the sorption step, and released to form oxygen vacancies in the oxide during the desorption step. Unlike conventional zeolite-based sorbents used in industrial VPSA oxygen production applications, perovskite-based sorbents are 100% selective to oxygen adsorption and can produce nearly 100% oxygen purity in single stage operations. In its earlier developments, the process was referred to as Ceramic Autothermal Recovery (CAR) Process, and continuous oxygen production was to be achieved by several fixed beds operating in parallel, in a cyclic process [1].

Figure 1 - CAR Process Concept

Between 2005 and 2008, DOE sponsored the development and testing of the CAR Process for oxy-combustion systems under two separate cooperative agreements [2, 3]. Following bench-scale proof-of-concept, the goal of these projects was to perform pilot-scale testing of the process, when integrated with a coal-fired combustor to produce a CO_2-rich flue gas. The work was successfully concluded and the main conclusions from the work were that the specific perovskite ($La_{0.1}Sr_{0.9}Co_{0.5}Fe_{0.5}O_{3-\delta}$, LSCF1955) chosen for testing (a) did not have the desired sorption capacities, (b) the operating temperature (850 ºC) was too high, and (3) the kinetics of desorption were too slow [4-6]. All three impacted the overall process economics, and in that regard, the project team's main conclusion was that the potential for sorbent-based oxygen production technology to achieve significantly lower overall costs compared to cryogenic air separation was technically possible but required further development efforts in order to achieve in practice. Pending the development of more suitable higher performing sorbents, further development of the technology was abandoned.

Table 1 illustrates a comparison of sorbent properties used in the legacy work with those of materials recently formulated and tested at Arizona State University [6]. New perovskite ceramic sorbent materials undergo an endothermic order-disorder transition accompanying the exothermic oxygen sorption. The apparent heat of sorption is then a combination of the endothermic transformation and the exothermic sorption process. As described later this affords an opportunity to optimize the thermal effects associated with sorption and desorption lowering the overall energy requirements for overall sorbent-based oxygen separation process. The new materials have a 20-40% higher O_2 adsorption capacity, lower apparent heat of adsorption, up to 200ºC lower operating temperature, and faster oxygen desorption rates. Preliminary economic evaluations show that these improvements in sorbent properties result in a much better performance specifically for the production of O_2 enriched streams for coal gasification. Pure oxygen can be produced by using steam as the sweep gas, by the use of vacuum pumps or by using CO_2 sweep in

conjunction with a high efficiency cryogenic separation of CO_2 and oxygen [7]. As displayed in the Table 1 new perovskite ceramic sorbent materials with order-disorder transition have a 20-40% higher O_2 adsorption capacity, lower apparent heat of adsorption (80-140 kJ/mol lower), up to 200 ºC lower operating temperature, and up to two orders of magnitude faster oxygen desorption rates than those observed in legacy sorbents.

Table 1 - Comparison of sorbent materials used in the previous CAR process development and the new materials proposed for this project

	Legacy Sorbents	New Sorbents
Sorbent Type	Classic Perovskite	Perovskite with order-disorder transition
Operation Temperature °C	600-900	400-700
Apparent Heat of Sorption (kJ/mol)	80-180	0-40
Sorption Capacity (m mol/g)	0.25-0.32	0.30-0.45
Desorption Rate Constant (1/s)	$1.0\text{-}4.0\text{x}10^{-4}$	$0.5\text{-}2.0\text{x}10^{-2}$

As a part of this project, development of an oxygen production process based on the new sorbent materials was proposed.

2. Objectives

Goal of the proposed work was to demonstrate an advanced oxygen production technology based on new-conducting metal oxide ceramic sorbents which undergo an endothermic order-disorder transition during the exothermic oxygen adsorption step. By taking advantage of the synergic effects of these two we propose to lower the apparent heat of sorption thereby minimizing heat effects to affect cost-effective air separation. Specific objectives were:

- Develop and Characterize an Improved Sorbent Chemistry Based on Mixed-Conducting Metal Oxide Ceramic Materials
- Develop a cost effective way to make robust sorbent pellets from an optimized chemistry, and characterize performance.
- Evaluate Sorbent Performance as a Function of Operational Parameters, and
- Perform cyclic PSA experiments to demonstrate oxygen production using sweep gases such as He, N_2 and CO_2, and vacuum operations.

Western Research Institute (WRI) served as the project lead with Arizona State University (ASU) providing basic sorbent research support and LP Amina performing economic assessment of the sorbent-based oxygen separation technology. This report describes the results emphasizing the testing at a kg-size batches concluded at WRI including LP Amina's rudimentary economic evaluation. ASU subcontract report dealing with TGA-based sorbent capacity and sorption/desorption kinetics characterization with mg- and g-size samples and development of alternate sorbent chemistries is detailed in Appendix A.

3. Results

3.1 Perovskite Sorbents with Oxygen Vacancy Order-Disorder Transition: Our interest in these materials is to utilize order-disorder phase transition to enhance oxygen sorption/desorption rate. Since oxygen is a more desirable product in most industrial process and the perovskite metal oxides only adsorb oxygen, the key to employ these materials practically is the desorption efficiency. Early research conducted by Yin et al. [4,8,9] showed that with disorder-to-order phase transition, the oxygen desorption rate was

significantly enhanced. Since during the desorption process the phase of the perovskite oxide transforms from disordered phase to ordered phase, we define it as disorder-order transition, while order-disorder transition take place during the subsequent sorption process. A list of sorbent materials exhibiting the order-disorder transition is displayed in Table 2. Among these sorbents, LSCF1991 has highest oxygen adsorption capacity at 500-600°C and fastest oxygen desorption rate (all these sorbents have fast oxygen sorption rates). Thus, our initial effort was to focus on measurements and analysis of oxygen sorption and kinetic data on LSCF1991 sorbent.

Table 2. Characteristics of Sorbents with Oxygen Vacancy Order-to-Disorder Transition

Sorbent	$SrCo_{0.8}Fe_{0.2}O_{3-\delta}$ (SCF82)	$La_{0.1}Sr_{0.9}Co_{0.9}Fe_{0.1}O_{3-\delta}$ (LSCF1991)	$SrCoFeO_{3-\delta}$ (SCF111)
Operation temperature (^{o}C)	400-700	500-700	700-800
Apparent heat of adsorption (kJ/mol)	0-40	0-20	N/A
Oxygen sorption capacity (mmol/g)	400--0.48	500--0.55	600--0.29
	500--0.34	600--0.45	700--0.27
	600--0.32	700--0.37	800--0.42
	700--0.23		900--0.41
Oxygen desorption rate (1/s)	$0.5\text{-}2x10^{-2}$	$0.2\text{-}1x10^{-2}$	$0.5\text{-}3x10^{-2}$

Figures 2 and 3 show oxygen adsorption isotherms and isobars on LSCF1991 obtained in our lab. This adsorbent does not adsorb nitrogen. As shown in Figure 2, below 700ºC where order-disorder transtion occurs with change of oxygen pressure, pressure swing may give higher adsorption capacity with a faster adsorption and desorption rate. It is important that the pressure swing is carried out in the pressure ranges that oxygen-vacancy order-disorder transition takes place.

Isobar data given in Figure 3 are interesting. At oxygen partial pressures above 0.03 atm, increasing temperature lowers amount of oxygen adsorbed, so the conventional temperature swing process may be used. However at pressures lower than 0.03 atm, increasing temperature may result in a jump in oxygen adsorption amount (at the transition point), followed by a decrease in oxygen adsorption amount with increasing temperature. The conventional thermal swing process would not work in this regime.

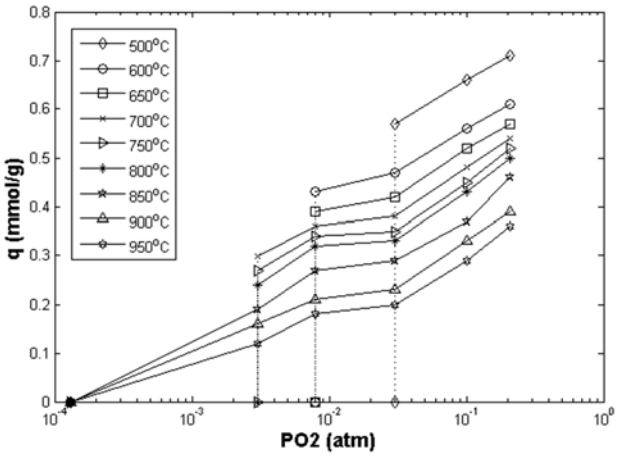

Figure 2. Oxygen sorption isotherms of LSCF1991

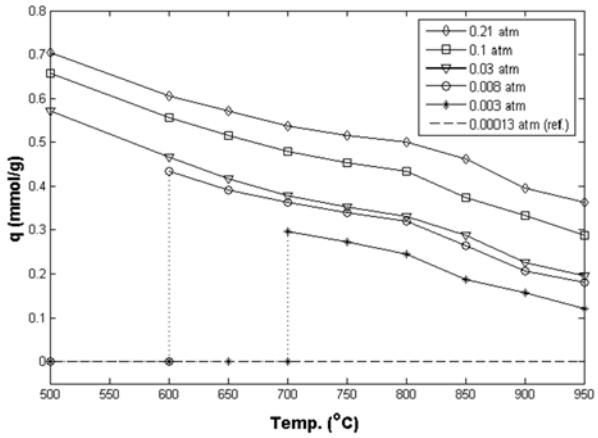

Figure 3. Oxygen sorption isobars of LSCF1991

Without order-disorder transition, the heat for oxygen adsorption in LSCF1991 is about

$$\Delta H_{sorp}=-185 \text{ kJ/mol}$$

the minus sign indicates exothermic heat in oxygen sorption, with "mol" means oxygen adsorbed. If there is order-to-disorder transition in oxygen sorption step, the endothermic heat of transition is:

$$\Delta H_{trans}=60 \text{ kJ/g}$$

So for a pressure swing process involving oxygen vacancy order-disorder transition, the modified heat for oxygen adsorption is:

$$\Delta H_{Modifed}=\Delta H_{trans}+ \Delta H_{trans} /q \qquad (1)$$

where q is the amount of oxygen adsorption (in unit of mol/g not mmol/g), and $\Delta H_{Modifed}$ has unit of kJ/mol.

If we use the following linear driving force model to describe the sorption or desorption kinetic:

$$\frac{dq}{dt} = k(q_e - q) \qquad (2)$$

Integration gives:

$$\frac{q}{\Delta q} = [1 - \exp(-kt)] \quad (3)$$

sorption or desorption rate constant can be estimated from the half-weight change time $t_{1/2}$ (time at $q/\Delta q = 0.5$) from the transient uptake curves. Typical results are given in Table 3. The temperature for without-transition process is around 800ºC and that for with-transition process is 700ºC. As shown, the oxygen desorption rate is about 2 orders of magnitude lower than the oxygen adsorption rate when there is no oxygen order-disorder transition. In the case with the transition, the oxygen desorption rate is much higher and becomes the same as the oxygen sorption rate.

Table 3. Oxygen sorption and desorption rate constants on LSCF metal oxide sorbent

	Without transition	With transition
Adsorption k (1/s)	$1.4\text{x}10^{-2}$	$1.4\text{x}10^{-2}$
Desorption k (1/s)	$3.5\text{x}10^{-4}$	$1.4\text{x}10^{-2}$

3.2 Sorption/Desorption Breakthrough Measurements: A lab-scale fixed-bed experiment setup was assembled to perform sorption breakthrough measurements on various sorbents. The set-up

comprises of two mass flow controllers, a four-way valve and related pipe fittings, a tubular furnace, a dense alumina tube packed with silica grain and sorbent, and an oxygen analyzer. A simple layout of the setup is illustrated in Figure 4. Before it was used for the sorption/desorption experiment, the dead volume of the system was tested by using an alumina tube packed with only silica grain. The results showed that the dead volume of the system is about 15 ml.

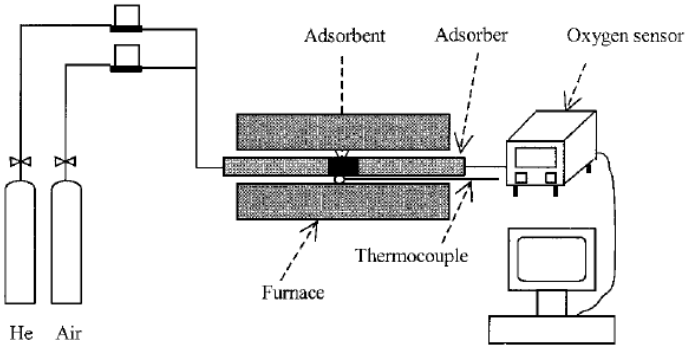

Figure 4. ASU's Fixed-bed setup layout

The operation conditions of the fixed-bed experiment were: both air and helium (purge) were set to be 5 ml/min under 1 atm, 2 grams of LSCF1991 powders were packed, the packing length was about 4 cm, and a thermocouple probe was placed in the middle of the sorbent pack. Breakthrough experiments were conducted at various temperatures. Figure 5 shows the sorption breakthrough curves at different temperatures in the 400-800°C range.

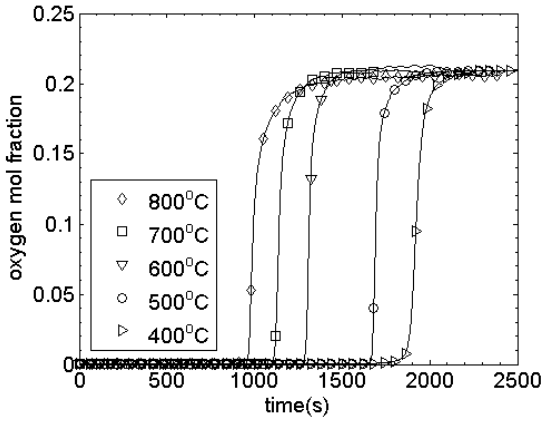

Figure 5. LSCF1991 sorption breakthrough curves

Sorption data from the fixed bed testing is compiled and compared with the TGA data for LSCF1991 in Table 4. Note that with the exception of 800°C, all other fixed-bed data are accordant with TGA. The trend that sorption capacity increases with decreasing temperature is quite obvious.

Table 4. LSCF1991 Sorption data from fixed-bed and TGA measurements

Temperature(°C)	Sorption Capacity (mmol/g)	
	Fixed-bed	TGA
400	0.645	0.641
500	0.569	0.544
600	0.467	0.460
700	0.378	0.388
800	0.325	0.291

Corresponding desorption breakthrough curves from fixed-bed testing are shown in Figure 6 and the amount of oxygen desorbed in one hour and two hours of desorption time with He sweep is compiled in Table 5. Unlike the sorption capacity which varied with temperature, the desorption amount and efficiency does not change much with the temperature. Although it is certainly lower at 800°C compared with other conditions, the results at 500°C to 700°C are very close. In the first hour of desorption, the desorption amount increase with decreasing temperature.

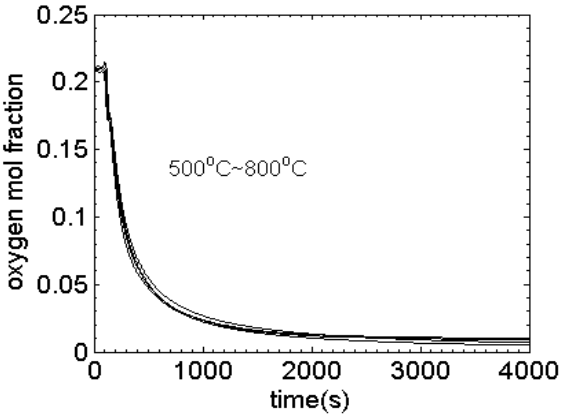

Figure 6. LSCF1991 desorption breakthrough curves

Table 5. LSCF1991 desorption data

Temperature(°C)	1hr desorption amount(mmol/g)	1hr desorption efficiency	2hr desorption amount(mmol/g)	2hr desorption efficiency
500	0.167	29.3%	0.205	36.0%
600	0.162	34.2%	0.217	45.8%
700	0.161	42.6%	0.212	56.1%
800	0.142	43.7%	0.165	50.8%

The temperature change of LSCF1991 bed undergoing sorption/desorption processes were recorded by a thermocouple. Figure 7 shows the temperature change during the sorption process at different temperature. The temperature change is very accordant with DSC data [4]. Begin with from 400°C, the trend of heat

released decreases as the temperature increases. To 700°C, there is only minimal heat effect. At 800°C, the process turn to endothermic, which is regarded as an evidence of phase transition.

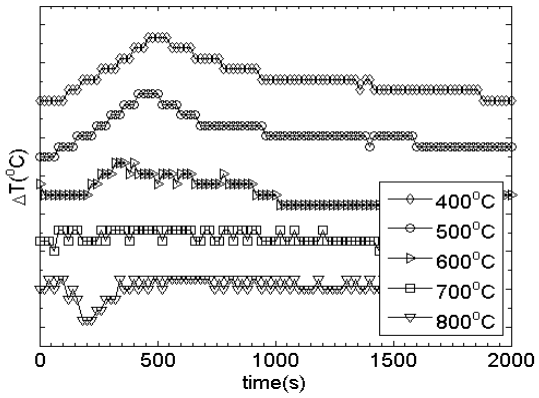

Figure 7. Temperature change during LSCF1991 sorption process (Each single tick on y-axis represents 1°C)

The fact that LSCF1991 exhibits the order-disorder phase transition can be seen in Figure 8. The figure shows the TGA-based desorption curves at various temperatures in the 400-800°C range. The onset of transition manifests itself as a sharp change in desorption rate. At temperatures where the transition exists, the process reaches equilibrium much faster than those without phase transition. Moreover, the desorption rate is not in a monotonic trend with increasing or decreasing temperature. When compared with fixed-bed results shown earlier in Figure 5, the two behavior do not seem to agree with each other.

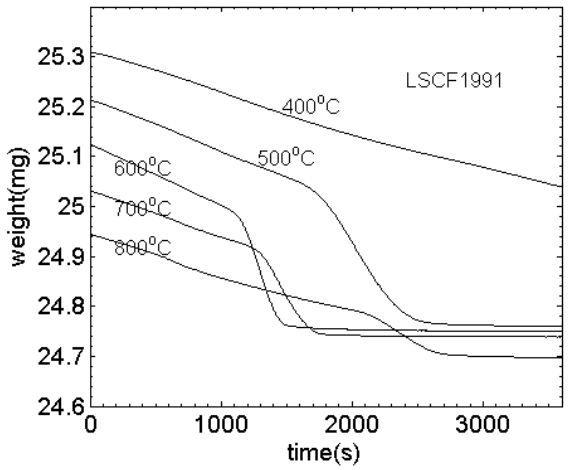

Figure 8. LSCF1991 TGA desorption curves

ASU researchers conducted an extensive analysis of the origin of the discrepancy observed in the TGA- and fixed-bed-based desorption measurements. The detailed explanation can be found in Appendix A. The appendix also summarizes our efforts to develop an improved sorbent chemistry.

3.3 Bench-scale PDU Testing: Several kg-size batches of sorbents were prepared following the recipe and procedure prescribed by ASU. The materials prepared were used to develop a pelletizing scheme. Using water and glycerin as a lubricant/binder additive, followed by a calcination and sintering step, extruded pellets were prepared (Figure 9). Sorbent pellets from the legacy work completed under previous cooperative agreements are also available for testing and were retrieved from the sample archives and were used to compare performance of the new sorbent chemistries.

Figure 9. Extruded Sorbent Pellets of LSCF 1991

Sorbent testing skid from the legacy projects from 2008 program was refurbished and upgraded. A photograph of the assembly is shown in Figure 10. The equipment was assembled such that the set-up could be readily reconfigured for partial pressure swing, or vacuum-pressure swing configurations. A schematic of the skid set-up for sweep gas and vacuum desorption configurations are displayed in Figures 11 and 12.

Figure 10. Fixed Bed Sorbent Evaluation Skid

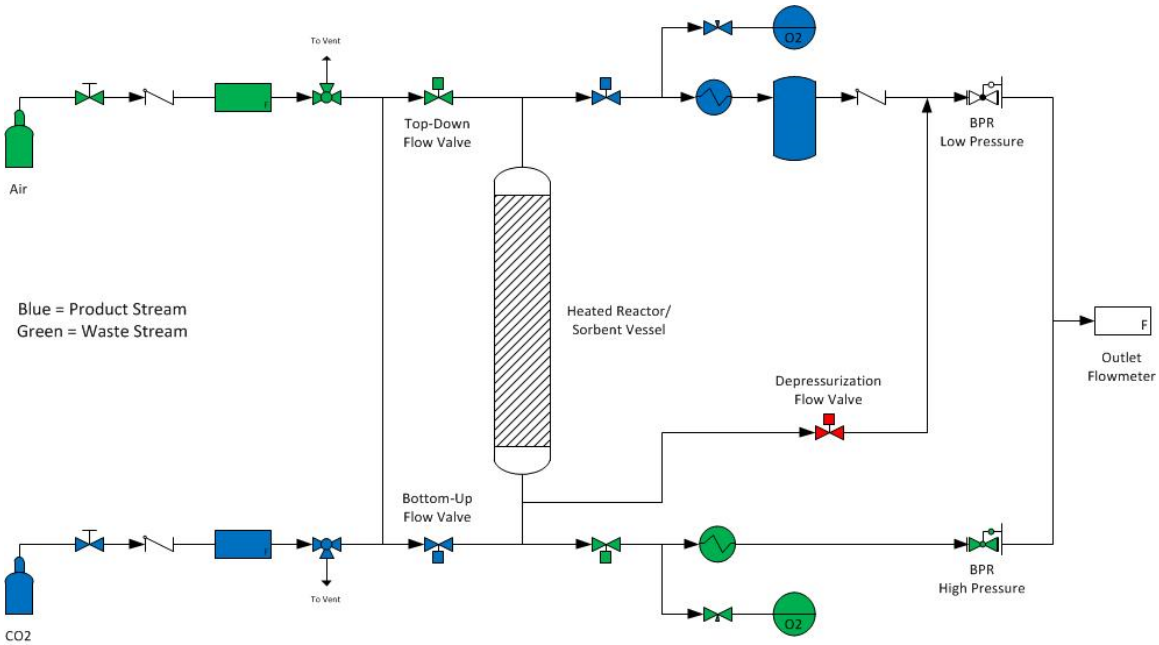

Figure 11. PFD of test set-up for partial pressure swing with sweep gas(es) testing of sorbent

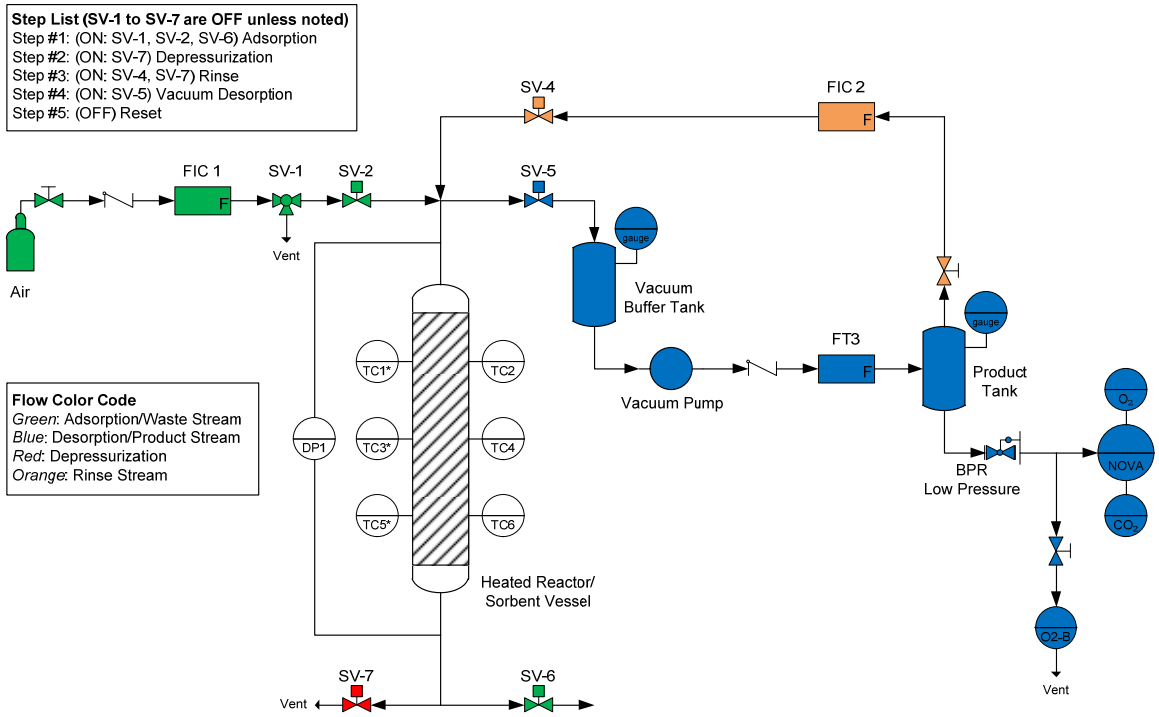

Figure 12. PFD for pressurized sorption/vacuum desorption cycle testing of sorbent

Two different reactors were assembled; 1”- and a 2”-diameter cylindrical fixed-bed reactors can be loaded with up to 12” deep sorbent beds. The sorbent bed is well instrumented such that up to seven TCs can monitor the bed temperatures. The test set-up has PC-based logging and controls capabilities. Figures 13 shows a pair of screen captures from a partial pressure swing test run with CO_2 sweep underway at 550° C.

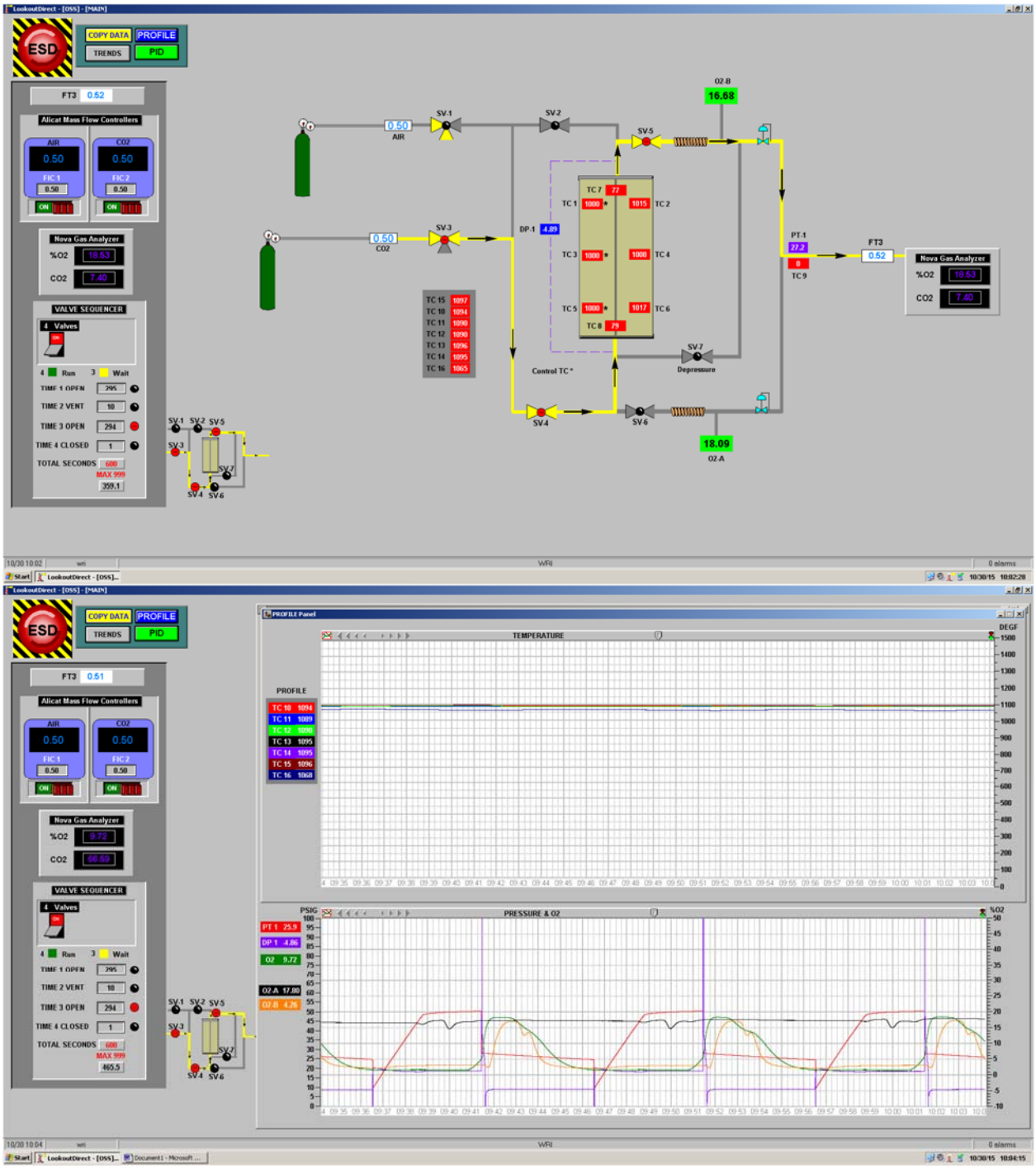

Figure 13. Screen captures from the process control PC. All process variables such as temperature, pressure, sweep gas rates, and cycle times can be controlled from various screens

A typical sorption/desorption test log is displayed in Figure 14. The figure shows a 5-minute sorption and 5-minute desorption cycle. Sorption cycle involved pressurizing the reactor to 60 psi. The reactor controls are set-up such that pressurization occurs quickly (about 30 seconds in Figure 14) by introducing air into the system at a higher flow-rate (5 slpm) and then slows down to a slower rate (1 slpm). Both the rates are operator selectable. In Figure 13 the duration of the sorption cycle is 5 minutes. Oxygen concentration of

the air exiting the reactor is continuously logged and in Figure 14 it shows a minimum at about 8% and fully recovers to about 20% near the end of the sorption cycle. For desorption, air flow to the reactor is stopped. Reactor pressure is relieved by venting to the atmosphere and a sweep flow (Air, He, or CO2 at 0.125 slpm) is initiated. Oxygen content of the sweep flow and the total flow exiting the reactor are logged. In subsequent discussion, we shall use "O_2 Min" and "O_2 Max" as defined in the Figure 14 as a measure of the sorbent performance under different temperature and pressure conditions.

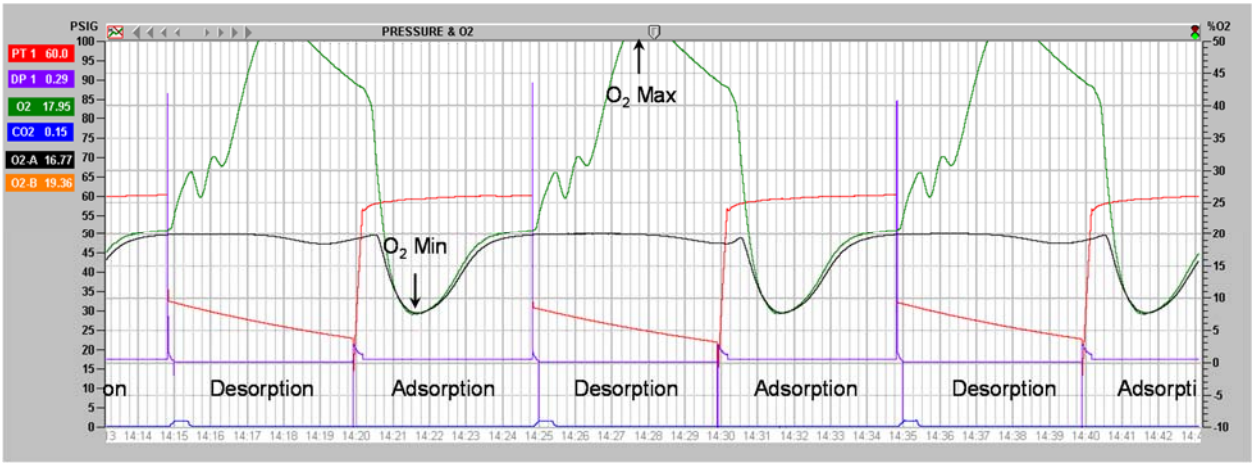

Figure 14. Screen capture of typical sorption/desorption performance recording from the control PC. Labels are added to the photograph to describe the data.

Temperature data are continuously logged. An example is shown in Figure 15. Figure shows the reactor and furnace temperature trends during a sorption/desorption test. Reactor temperature clearly shows temperature changes afforded by the sorption and desorption reactions similar to those described earlier in Figure 7. Change in temperature from desorption to sorption, ΔT is a reflection of the adsorption exotherm proportional to the amount of oxygen adsorbed by the sorbent.

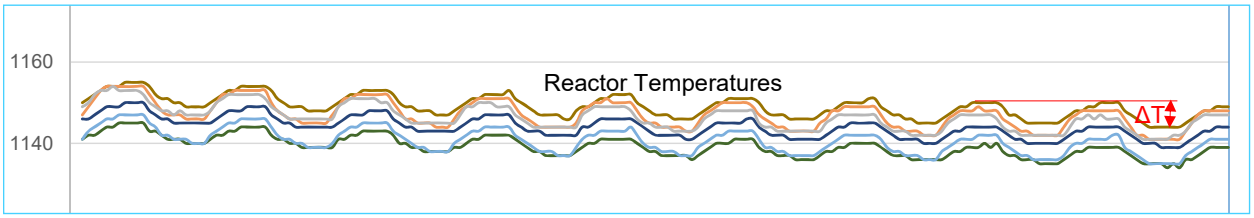

Figure 15. Reactor temperature during cyclic sorption/desorption testing

Tests were completed with LSCF 1991 and LSCF 2864. Temperature range explored is 900 – 1350 ºF (482–732 ºC), and at sorption pressures up to 80 psi.

As an example of the data collected, Figure 16 summarizes the performance of LSCF 2864 at 1050 ºF (566 ºC). The figure shows O_2 Max and O_2 Min for air, He and CO_2 sweeps. In all cases the sweep gas carried a greater than 55% O_2. When the gases were collected in a reservoir, average oxygen content of the gas approached 50%. Temperature dependence of the sorbent performance are illustrated in Figures 17.

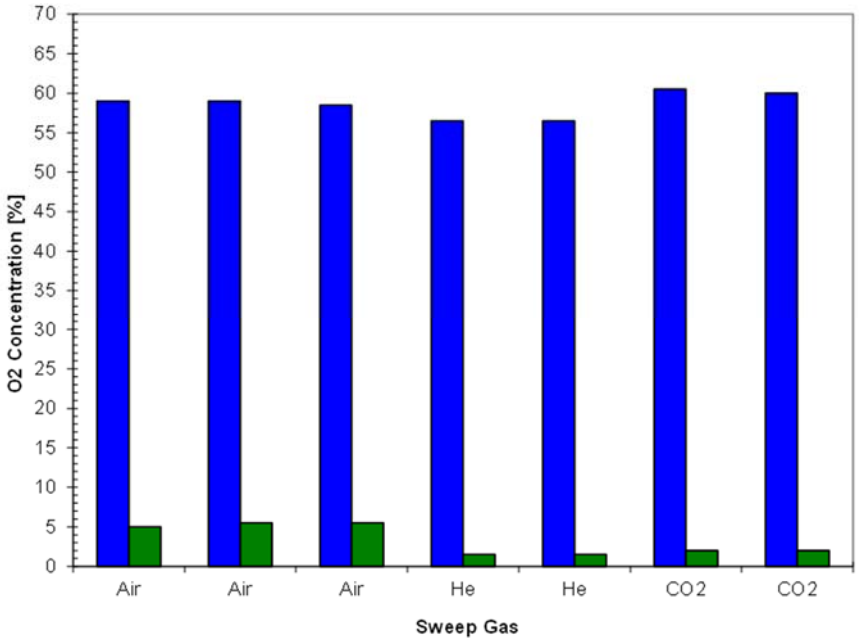

Figure 16. Sorption/Desorption Performance of LSCF 2864 under various sweep gas conditions at 1050 F (566 C)

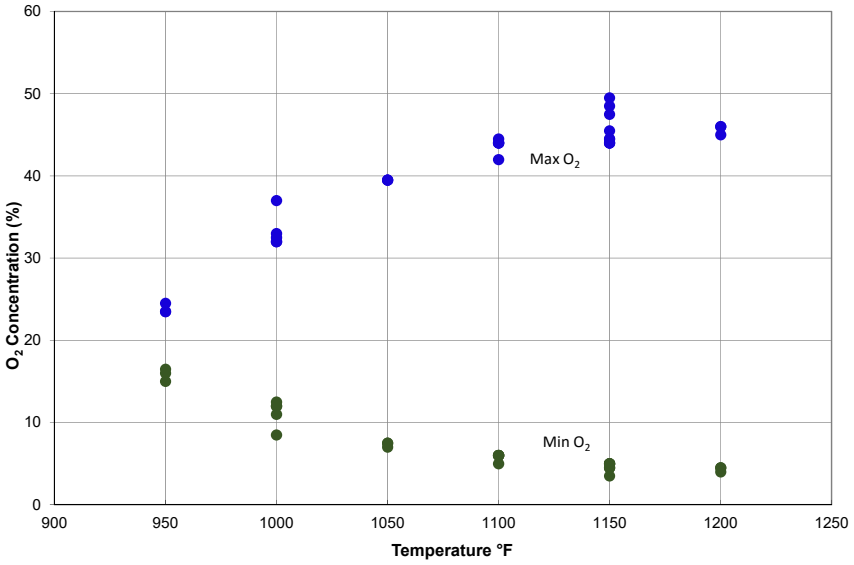

Figure 17. Sorption/Desorption Performance of LSCF 1991 at various temperatures (55 psi sorption pressure; 7 psi desorption pressure with He sweep)

Similar test was also conducted with LSCF 1991 with CO_2 sweep gas. However, the performance of the sorbent was observed to deteriorate with time (Figure 18). The performance degradation is related to the carbonation reaction. Increasing the La content of the sorbent such as in LSCF 2864 or LSCF 2891 retards this reaction. In our tests, no such deterioration was observed in LSCF 2864. We would like to point out

that the deterioration in performance is reversible. Simply by switching to air-sweep or He-sweep, we were able to rejuvenate the LSCF 1991 back to its original performance under both the air and He sweeps.

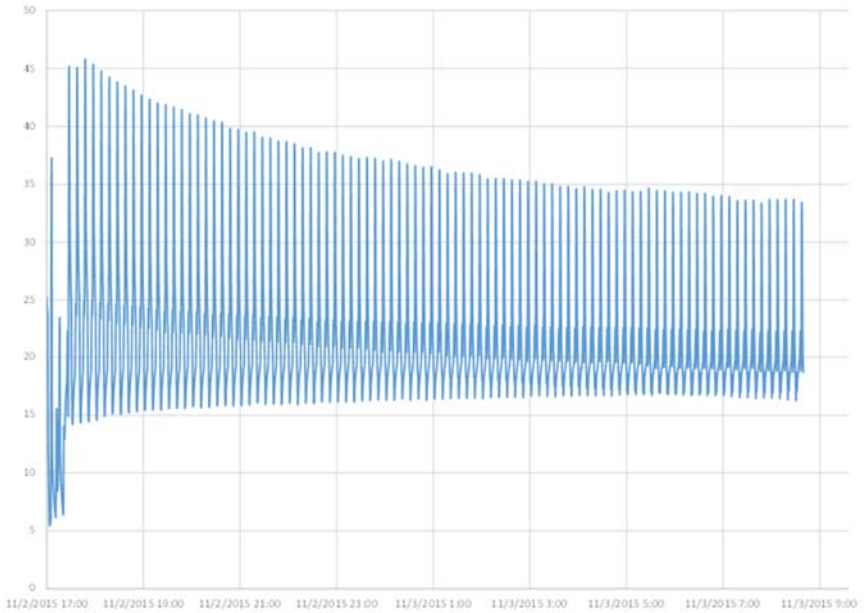

Figure 18. LSCF 1991 sorption/desorption trend for an extended operational test

To underscore the sorbent performance improvement, Figure 19 shows a simple comparison of oxygen concentration in the CO_2 sweep gas. In earlier testing, in support of oxy-combustion, highest concentration of oxygen in the sweep gas achieved was around 12% at an operating temperature of around 850 ºC. In our tests, we have been able to achieve nearly 60% peak concentration at an operating temperature of 565 ºC.

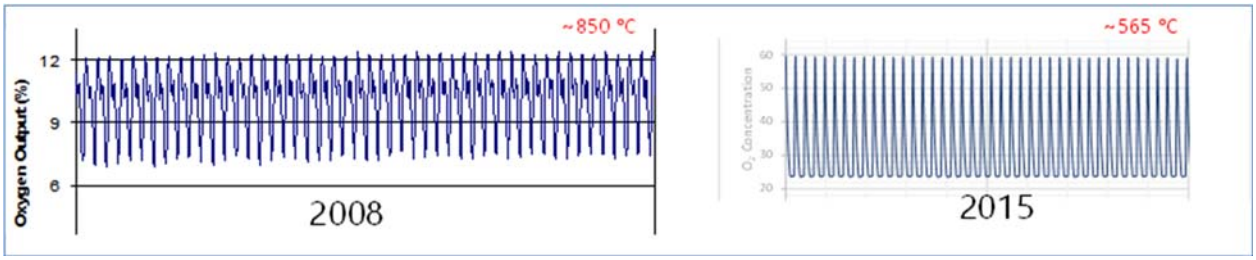

Figure 19. Sorbent performance as observed in 2008 compared to recent data

Using steam as the sweep gas and then condensing the water out of the product oxygen stream is a possible route. However, materials compatibility and the thermal penalty associated with the heat of vaporization and condensation are the two major issues with this approach. We proposed to use vacuum pressure swing as an alternative for producing "pure" oxygen. In that spirit, as stated earlier, the test equipment was assembled to allow for simple switch between partial pressure swing, and vacuum-pressure swing configurations.

A series of vacuum desorption tests was conducted with LSCF 2864 at various temperatures and pressures. Fixed bed of sorbent underwent adsorption at a fixed pressure and temperature and then desorption occurred by exposing the sorbent bed to a vacuum. The gas exiting the vacuum pump was analyzed for its oxygen concentration. The O_2 concentration data are displayed in Figures 20 and 21 for temperature and pressure

dependence respectively. Figure 20 shows the Oxygen concentration of product gas as a function of temperature. The adsorption pressure used was 40 psi. Similarly, Figure 21 shows the data as a function of pressure at a temperature of 1000º F.

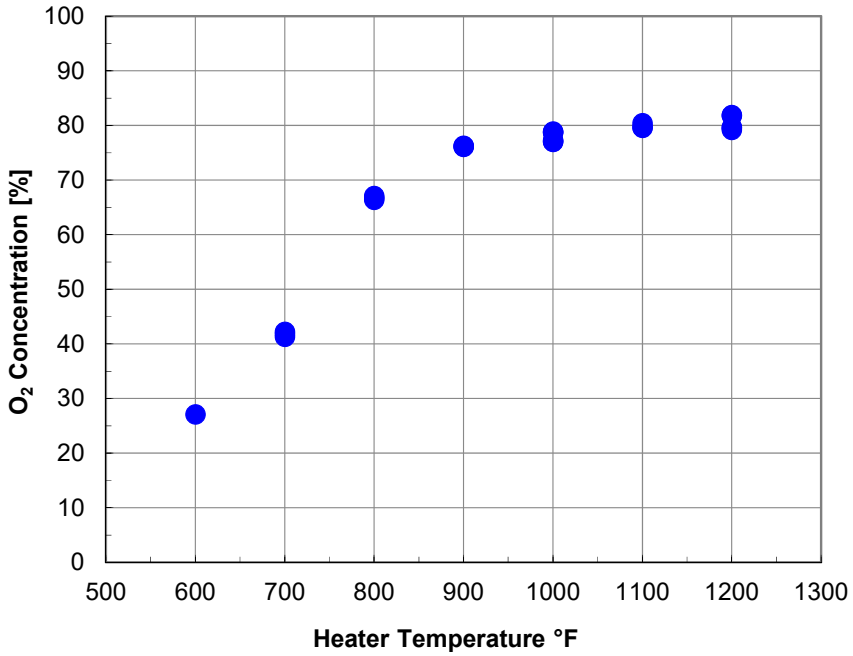

Figure 20. O_2 content of the product gas as a function of sorption temperature (Sorption P = 40 psi)

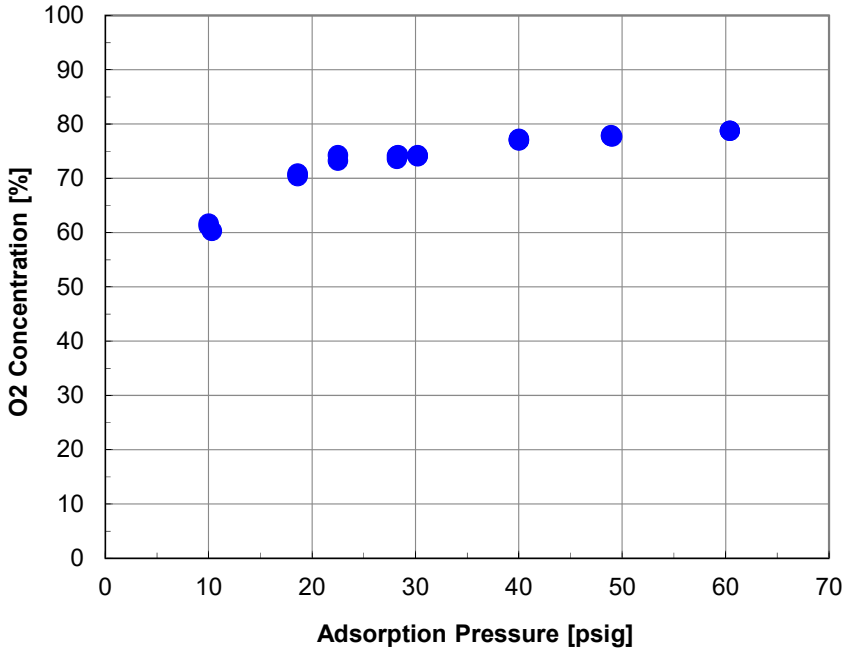

Figure 21. O_2 content of the product gas as a function of sorption pressure (Temperature = 1000º F)

Data shown in Figures 20 and 21 underscores the need for a rinse or a purge between the pressure adsorption step and the vacuum desorption step to produce oxygen with a higher purity than about 80% or so. The

limitation arises from any in-leaks during vacuum operation, the dead volume in the set-up and void volume in the sorbent bed. In principle, once all the leaks are removed, if we can impose a rinse cycle between adsorption and desorption steps to remove depleted air from the void volume of the sorbent bed, vacuum desorption should produce "pure" oxygen. In our tests, the equipment modifications required to affect the changes, required considerable effort in (1) reducing the dead volume in the system, (2) elimination of in-leaks, and (3) development and optimization of an appropriate rinse or a purge methodology.

One of the approaches for a rinse cycle is shown earlier in Figure 11, the gas used for rinse is the oxygen product itself. The steps involving various valves in the PFD are tabulated in the inset in the figure and include: (1) adsorption, (2) depressurization, (3) Rinse, and (4) vacuum desorption. Several tests were conducted to optimize the times for each one of these steps to produce 95% pure oxygen (Table 6). The Table compiles a list of test conditions with associated oxygen purity achieved. We would hasten to add that several other variables such as reactor size and shape, sorbent pellet size and shape including void volume and reactor dead volume, flow rates, operating temperature and pressures enter into the cycle optimization. The data displayed in the table is cited as an example to achieve the desired product quality.

Table 6. Cycle Optimization Tests

Test No.	T, °F	Pressure, psi	rinse	cycle	yield, %	$[O_2]$,%
1	1000	0	atm	178/1/1/179	8.7	49.4
2	1000	0	vac	178/1/1/179	3.1	65.4
3	1000	0	vac	178/1/11/179	2.6	64.7
4	1000	10	vac	298/1/1/179	9.8	87.9
5	1000	10	vac	298/1/1/119	11.3	88.4
6	1100	10	vac	298/1/1/119	11.4	89.6
7	1200	10	vac	298/1/1/119	11.9	90.1
8	1200	20	vac	298/1/1/119	14.4	91.1
9	1200	20	atm	298/1/1/119	19.0	80.6
10	1000	0	atm	298/1/1/119	7.9	52.8
11	1200	20	atm	298/1/1/119	18.7	81.4
12	1300	20	atm	298/1/1/119	19.3	82.4
13	1300	20	vac	298/3/1/119	13.6	94.5
14	1300	20	vac	298/7/1/119	12.9	95.1
15	1300	20	vac	298/1/1/119	14.5	94.6
16	1300	20	vac	118/1/1/119	13.9	89.4
17	1300	20	vac	118/1/1/59	17.1	90.4
18	1300	20	vac	88/1/1/29	20.7	88.8
19	1300	20	vac	88/2/1/29	19.6	89.0
20	1300	20	vac	88/4/1/29	18.3	88.7
21	1300	20	vac	298/3/1/119	13.6	95.1
22	1300	20	vac	298/3/1/60	14.7	95.2
23	1300	20	vac	299/3/1/40	14.8	95.9
24	1300	20	vac	299/3/1/30	14.5	94.7
25	1300	20	vac	300/2/1/40	14.5	95.0

3.4 Numerical Simulations: A ProSim adsorption process simulation module was used for adsorption breakthrough simulation on LSCF-1991. The oxygen adsorption equilibrium and kinetics data presented section 3.1 were used for the simulations.

Based on the oxygen adsorption isotherm data for LSCF-1991, we used Freundlich-Heller model for oxygen adsorption fitting, which is

$$q_i = K_0 * \exp(K_1/T) * (P_i\text{^}(1/n))$$

where K_0 (mol/g/atm) and K_1 (K) are constants.

Table 7 and Table 8 display the model parameters determined at 700°C and 900°C. We compared the adsorption isotherm and the fitting plot in Figure 22 and Figure 23.

Table 7. Model parameters determined at 700°C

K_0	K_1	n	R^2
0.592	-1.16E-04	7.457	0.93

Table 8. Model parameters determined at 900°C

K_0	K_1	n	R^2
0.429	-8.38E-05	4.543	0.93

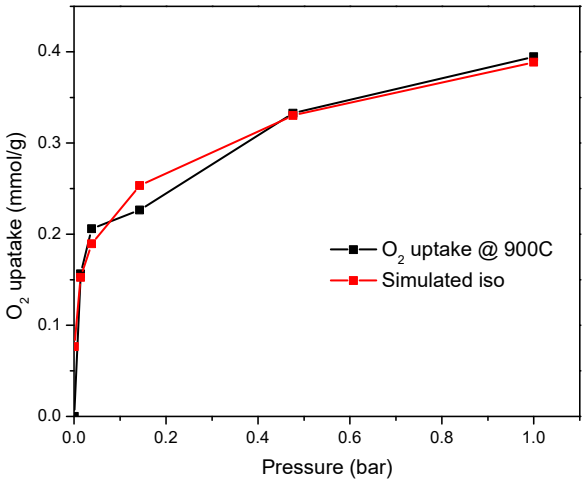

Figure 22. Oxygen adsorption isotherm and simulated isotherm at 700°C

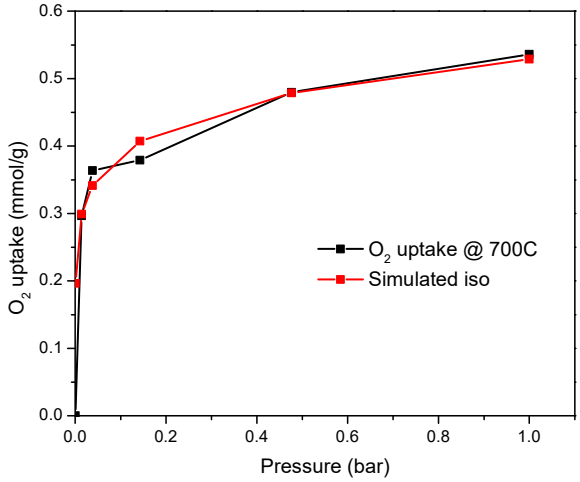

Figure 23. Oxygen adsorption isotherm and simulated isotherm at 900°C

Clearly, the agreement between the simulation results and the laboratory data are excellent.

Breakthrough simulations were conducted at various temperatures, flow rates and sorbent mass to find their effect on the breakthrough curve. Initial specifications for the calculations are listed in Table 9.

Table 9. Initial Simulation Specifications

i. diameter	6 mm
o. diameter	9 mm
packing length	5 cm
Adsorbent	LSCF-1991
Adsorbent mass	3.4 g
Adsorbent density	5.72 g/cm^3
Void fraction	0.3
Flow rate of air	10 mL/min
Feed Ration (mol:mol)	21:79 (O_2:N_2)

Figure 24 shows the oxygen and nitrogen simulated breakthrough curves obtained under the initial simulation specifications at 700°C and 900°C. An earlier breakthrough point was reached at a higher temperature. This is reasonable based on the fact that higher temperature caused a faster transport due to an increase in diffusion coefficient.

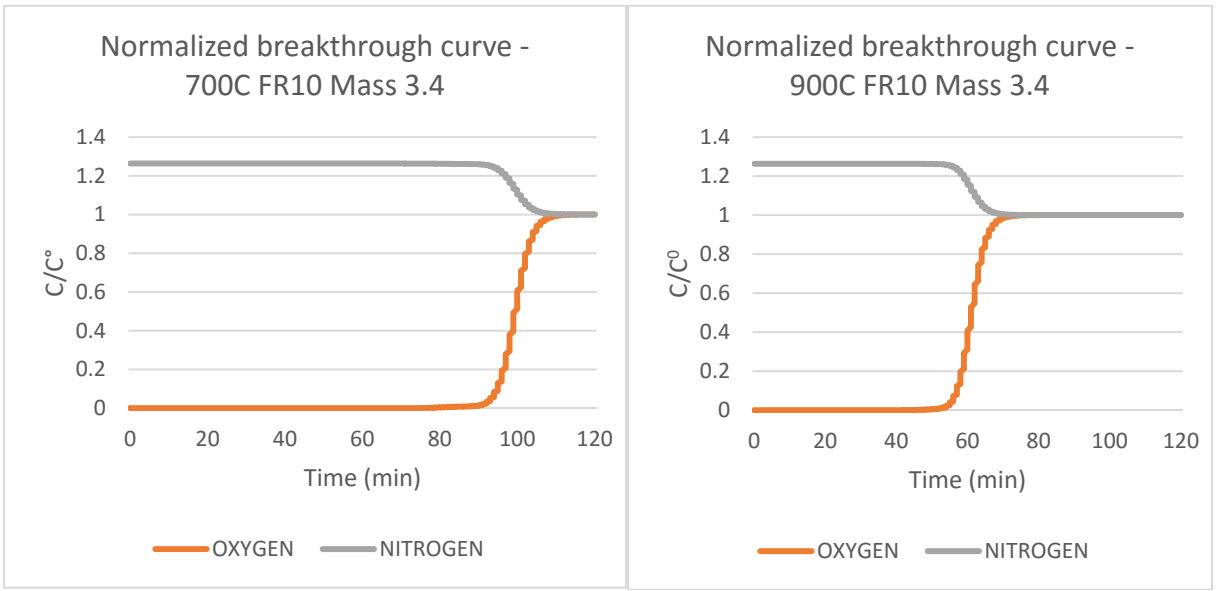

Figure 24. Simulated breakthrough curves for oxygen and nitrogen under the initial simulation specifications at 700°C and 900°C

The effect of air flow rate on the adsorption of oxygen on LSCF-1991 was investigated by varying the air flow rate (5, 10, 15, and 20 ml/min) with constant adsorbent mass of 3.4 g at 700°C, as shown by the oxygen breakthrough curves in Figure 25. We can see at a higher flow rate of air, the adsorption zone quickly

reached the top of column and the column was saturated earlier. The steeper curve with earlier breakthrough and exhaustion time resulted in less adsorption uptake.

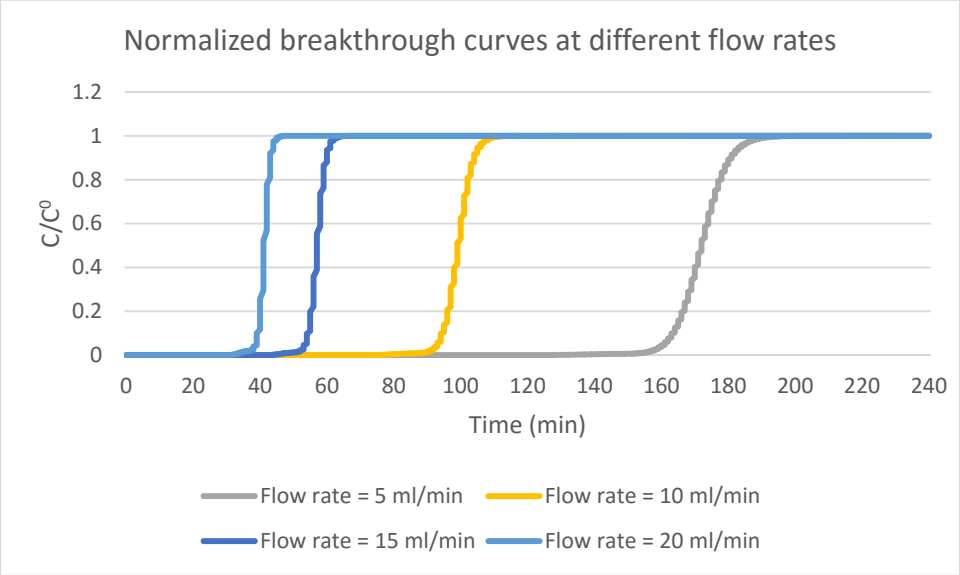

Figure 25. Oxygen breakthrough curves at different flow rates (5, 10, 15, and 20 ml/min)

We also analyzed the effect of adsorbent mass by varying the adsorbent mass (2, 3.4 and 5 g) with constant air flow rate of 10 ml/min at 700°C. As can be seen from Figure 26, with the increase of adsorbent mass, the breakthrough time increased at first but then decreased. With an adsorbent mass of 3.4 g, the breakthrough curve indicated the largest adsorption uptake. The increase of adsorbent will provide more oxygen vacancy sites for the adsorption process, but too much adsorbent will prevent air flowing through the column due to a constant column configuration.

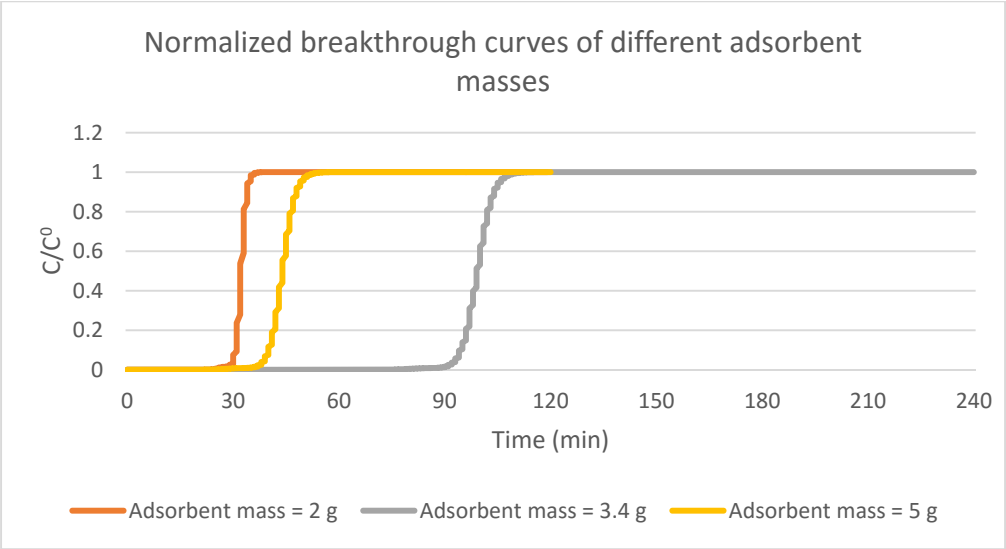

Figure 26. Oxygen breakthrough curves at different adsorbent masses (2, 3.4, and 5 g)

The breakthrough experiments by sorption of oxygen on LSCF 1991 pellets were performed in a fixed bed. The fixed-bed setup included an adsorber column, a heat insulation tube, a gas delivery system, an oxygen analyzer, and a data record system. Oxygen concentration of the exhaust gas was measured by the oxygen

analyzer, so the sorption and desorption breakthrough data were recorded, which help to analyze the fixed-bed adsorption behavior. The breakthrough experiment data of LSCF-1991 pellets was then compared with simulation result. The experimental and simulated breakthrough curves at two different temperature are compared in Figure 27 and Figure 28.

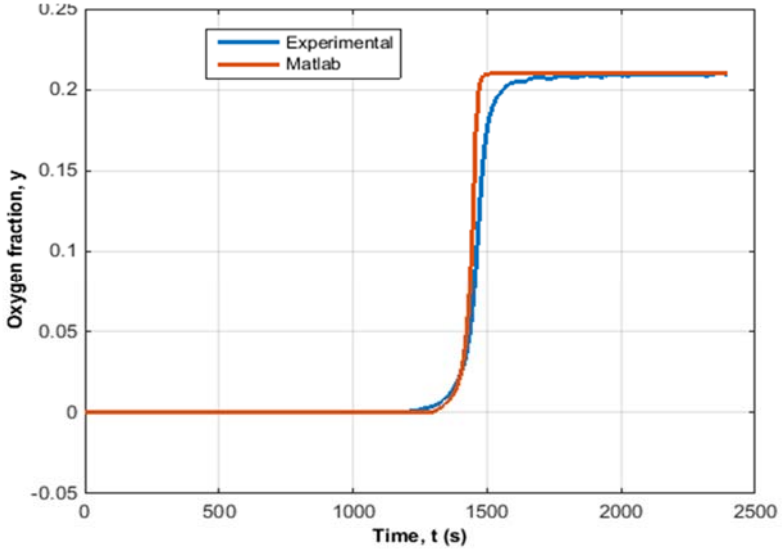

Figure 27. Experimental and simulated breakthrough curves at 500 ºC

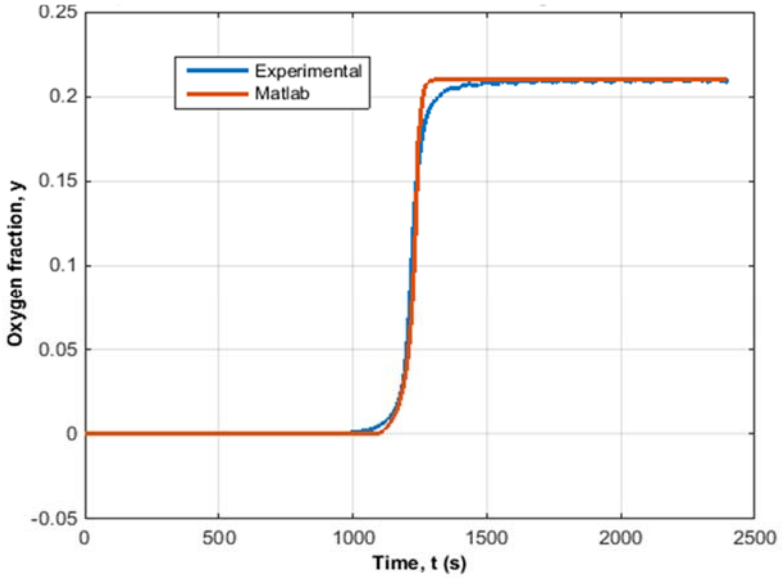

Figure 28. Experimental and simulated breakthrough curves at 600 ºC

From the above figures, the simulated breakthrough curves are very close to the experimental curves. Therefore the simulation code is deemed ready for use in further design and development of the adsorption process.

To study the effect of feeding pressure, cycle time and packing length, several parallel simulations were performed as shown in Table 10. For all trial simulations, oxygen purity is calculated at the end of 6th

cycle. For cycle time, pressurization and depressurization steps are included in adsorption and desorption separately. Pressurization time is 5 seconds and depressurization time is 1 second.

Table 10. Simulation Table

No.	Air pressure (psia)	Nitrogen pressure (psia)	Cycle time adsorption + desorption (s)	Packing length (in.)	Oxygen purity %
1	15	2	300 + 300	1.5	41.8
2*	20	2	300 + 300	1.5	44.7
3	30	2	300 + 300	1.5	48.7
4	40	2	300 + 300	1.5	51.4
5	20	0.1	300 + 300	1.5	44.7
6	20	1	300 + 300	1.5	44.7
7*	20	2	300 + 300	1.5	44.7
8	30	3	300 + 300	1.5	44.7
9*	20	2	300 + 300	1.5	44.7
10	20	2	150 + 300	1.5	44.9
11	20	2	300 + 150	1.5	52.1
12	20	2	150 + 150	1.5	51.9
13	20	2	240 + 60	1.5	58.5
14	20	2	150 + 30	1.5	60.0
15*	20	2	300 + 300	1.5	44.7
16	20	2	300 + 300	2.5	39.0
17	20	2	300 + 300	6	25.4
18	40	2	240 + 60	1.5	76.0

From the simulation result, the pressure of air, desorption time of a cycle, and packing length are the three main factors which affect oxygen purity, while the effect of pressure of purge gas and adsorption time of a cycle are insignificant. Oxygen purity increases with the increase of air pressure, and with the decrease of desorption time and packing length. With the preferred conditions, which is simulation No.18, oxygen purity reaches 76%. Qualitatively, the simulation results are consistent with the experimental data described earlier on the purity of the product.

3.5 Process Economics: We have prepared an economic model for sorbent-based oxygen production based on the following: experimental thermodynamic data generated from TGA measurements of the new perovskites, kinetics data generated from bench scale testing of the new perovskites together with Aspen™ process simulations and capital cost estimator. All were based on the following plant design and operational assumptions. All these assumptions were viewed a key input variables for the financial model and helped to guide cost optimization.

- Product Oxygen Purity, >98%
- Perovskite sorbent costs, $6,000/ton
- Two thermally integrated, close-coupled, equal size "reaction volumes" for sorption and desorption (Tube and shell reactor)
- Adsorber-Desorber Tubes, 100 mm dia. tubes
- 12 cycles per hour, 5 minute cycles
- Adsorption-Desorption Temperature: 550°C
- Adsorption Pressure: 7 psig
- Desorption Pressure: -7 psig
- Sorbent Performance: 0.001 - 0.002 g O_2/g sorbent per cycle
- Sorbent Pellets: 5mm x 1mm dia. pellets
- Blower productivity @ 7psig discharge pressure: 14.4 KW-hr power consumption per ton air feed
- Oxygen yield as a percent of air fed to adsorber: 50%

Two commercial cases were considered: 1) a large-scale oxygen plant, e.g., to supply an oxy-combustion or IGCC power station, and 2) a smaller scale oxygen plant, e.g. for an electronics fab or a small-scale 5MW coal fed IGCC facility. We used the preferred, current lowest cost technologies for comparison at each scale: A cryogenic oxygenic air separation unit (ASU) for the large scale benchmark (400,000 Nm^3/hr oxygen) and a vacuum pressure swing adsorption (VPSA) system for the smaller scale benchmark (2,500 Nm^3/hr oxygen). Table 11 below summarizes the estimated capital and operating costs for sorbent-based oxygen delivery at 2,500 Nm^3 O_2 per hour (94 ton O_2 per day) and at 400,000 Nm^3 O_2 per hour (15,000 ton O_2 per day).

Table 11 contains the list of major equipment along with installation cost estimates. For OPEX, we considered only electric power, equipment maintenance, and the sorbent make-up costs. Labor and SG&A were not included because we presume that these would be similar to the legacy, benchmark technologies. These numbers were rolled into the cost of oxygen and summarized in Table 12 below. It must be further noted that in all the LCO cases presented it is additionally assumed that the adsorber-desorber heating needs are essentially eliminated due to close coupling with high temperature IGCC and oxy-fired combustion processes.

Table 11. Capital Cost Estimates for Sorbent-based Oxygen Plant

	2,500 Nm3/hr O2 supply (small comm'l)		***400,000 Nm3/hr O2 supply (large comm'l)***	
	3.57 tonnes/hr		*572 tonne/hr*	
Equipment	Purchased Cost ($)	Installation Cost ($)	Purchased Cost ($)	Installation Cost ($)
Air blower	$32,400	$8,100	$5,184,000	$1,296,000
Adsorber/Desorber vessel	$940,000	$235,000	$58,311,000	$37,600,000
Sorbent	$1,506,000	$0	$240,960,000	$0
Vacuum Pump	$1,620	$405	$259,200	$64,800
Equipment Costs	**$2,480,020**	**$243,505**	**$304,714,200**	**$38,960,800**
Installed equipment cost	$2,723,525		$343,675,000	
+ Direct costs (Others)	$438,309		$28,689,390	
Total direct cost	**$3,161,834**		**$372,364,390**	
+ Indirect costs	$711,035		$46,540,566	
Fixed Capital Investment	**$3,872,869**		**$418,904,956**	

As a basis for comparison, we used publicly available information provided in reference 3. In general, we find that the LCO process has slightly higher capital cost than both the large ASU and the VPSA systems, but operational costs are lower. In order to make a cost of oxygen comparison, we assigned a capital cost of 8% per annum, and then divided by the tons of oxygen produced. As can be seen in Table 12 once we consider the cost of capital, the sorbent-based cost of oxygen is 26% lower than VPSA oxygen; and additionally the sorbent-based cost of oxygen is 13% lower than ASU oxygen. The source of the savings versus VPSA is in the fact that the desorber blower is about $1/5^{th}$ the size of a VPSA resulting in substantial energy savings. Not surprisingly, the advantages of LCO are less than a large-scale ASU because LCO numbers up for achieving scale and similar to VPSA does not enjoy as high economies of scale as cryogenic ASU processes do. It is noteworthy that VPSA is much more expensive than ASU at large scales, and becomes non-competitive with ASU technology around 100 tonne/hr, whereas LCO is projected to be cost-competitive with ASU for large scale applications. This is due to its more efficient use of waste heat (in the context of an IGCC or oxy-combustion system) and lower electrical consumption.

Table 12. Comparison of oxygen production costs

Oxygen capacity (Nm3/hr)	***2,500***		***400,000***	
System type	VPSA	LCO	ASU	LCO
Specific power required kWhr/tonne O_2	255	144	223	144
CAPEX $mio	4.43	3.87	377	419
Annualized cost of capital $mio	0.354	0.310	30.2	33.5
Maintenance (3% of capital), $mio	0.133	0.116	11.310	12.567
Cost of capital $/tonne O_2	11.3	9.9	5.48	6.7
Maintenance costs, $/tonne	4.2	3.7	2.3	2.5
Sorbent make-up costs, $/tonne O_2	Included	0.51	0	0.51
Electricity cost, $/tonne O_2	17.9	10.6	15.6	10.6
Total cost of oxygen $/tonne O_2*	**33.4**	**24.7**	**23.3**	**20.3**
% savings v. benchmark	***N/A***	***26%***	***N/A***	***13%***

** Does not include SG&A, direct labor (which should be similar in benchmark and LCO cases)*

4. Summary and Conclusions

As a part of a moderate-temperature sorbent-based oxygen production technology development project, a series of sorbent performance tests were conducted. Sorbent-based oxygen production process utilizes oxygen-storage properties of Perovskites to (1) adsorb oxygen from air in a solid sorbent, and (2) release the adsorbed oxygen into a sweep gas such as CO2 and/or steam for gasification systems or recycled flue gas for oxy-combustion systems. Pure oxygen can be produced by the use of vacuum instead of a sweep gas to affect the pressure swing. Tests confirmed that a new class of sorbents exhibiting a vacancy order-disorder transition during the adsorption/desorption process indeed offer a higher O2 adsorption capacity, moderate operating temperatures, and faster desorption rates.

The performance advancements afforded by the new materials lead to potential savings in capital investment and operational costs. Cost of producing oxygen using sorbents could be as much as 26% lower than VPSA system and about 13% lower than a large cryogenic air separation unit. Cost advantage against large cryogenic separation is limited because sorbent-based separation numbers up sorbent modules for achieving the scale up.

Few risks remain in terms of commercialization, one is sorbent life but these can easily assessed without great expense in follow-up studies, and should the sorbent material require periodic rejuvenation for continued re-use, these would not appear to be complex or costly operations.

Several upside benefits may also result from a continued technology development program. One is that the sorbent working capacity used in our techno-economic calculations was assumed to be less than about 10% of the total theoretical working capacity of the sorbent. Additional development may further improve the sorbent in order to utilize more of the oxygen sorption capacity. As such, both lower cost and lower quantity of sorbent could result in significant additional financial benefit.

5. References

1. Boer, Jurgen; Bulow, Martin; Guth, Hans Ulrich, "Oxygen sorbent compositions and methods of using same", US Patent Number 20050176589 A1.
2. D. Acharya, K.R. Krishnamurthy, M. Leison, S. Macadam, V.K. Sethi, M. Anheden, K. Jordal, and J. Yan, "Development of a High Temperature Oxygen Generation Process and Its Application to Oxycombstion Power Plants with Carbon Dioxide Capture", Proc. Of the 22nd Pittsburgh Coal Conference, Pittsburgh, Penn, Sept. 11-15, 2005.
3. K.R, Krishnamurthy, D. Acharya and F.R. Fitch, "Pilot-scale demonstration of a novel, low-cost oxygen supply process and its integration with Oxy-fuel Coal-Fired Boilers", Final Report, DOE Award Number:DE-FC26-06NT42748(2009). www.netl.doe.gov/File%20Library/Research/Coal/ewr/co2/42748-BOC-O2-supply-CAR-Final-Report_Dec-2008.pdf
4. Q. Yin and Y.S. Lin, "Beneficial effect of order-disorder phase transition on oxygen transport properties of perovskite-type oxides", Solid State Ionics, 178, 83-89 (2007)
5. H. Krudhof, H.H.M. Bouwmeester, R.H.E. v. Doorn, A.J. Burggaaf, "Influence of order-disorder transitions on oxygen permeability through selected nonstoichiometric perovskite-type oxides", Solid State Ionics, 63-65, 816-822 (1993).

6. Q. Yin, J. Kniep, Y.S. Lin, "High Temperature Air Separation by Perovksite-type Oxide Sorbents-Heat Effect Minimization", Chem. Eng. Sci., 63, 5870-5675 (2008).
7. Larry Baxter, http://sesinnovation.com/technology/carbon_capture/
8. Q. Yin, J. Kniep, Y.S. Lin. High temperature air separation by perovskite-type oxide sorbents-heat effect minimization. Chem. Eng. Sci. 2008, 63, 5870–5875
9. Q. Yin, J. Kniep, Y.S. Lin. Oxygen sorption and desorption properties of Sr–Co–Fe oxide. Chem. Eng. Sci. 2008, 63, 2211-2218
10. J. Hart, M. J. Battrum, and W. J. Thomas, "Axial pressure gradients during the pressurization and depressurization steps of a PSA gas separation cycle," Gas Separation & Purification, vol. 4, no. 2, pp. 97–102, Jun. 1990.

Appendix I
ASU Subcontract Report

Professor Jerry Lin

Sorbent-based Oxygen Production for Energy Systems

DE-F80024075

Final Report for ASU Subaward

Jerry Y.S. Lin
Arizona State University
Tempe, AZ85287

December 21, 2016

Abstract

LSCF perovskite oxides exhibit fast oxygen sorption rate and good oxygen adsorption capacity. Gravimetric experimental results show that the perovskite materials with disorder-to-order phase transition exhibit an oxygen desorption rate significantly faster than the materials without disorder-order phase transition. However, the disorder-order enhanced desorption rate is not observed in the fixed-bed desorption process. The oxygen partial pressure surrounding the sorbents is found to significantly affect the phase transition property. The oxygen partial pressure during the fixed-bed desorption process is above the equilibrium pressure of the ordered phase. Thus the phase transition only happens in the late stage of desorption during the fixed-bed oxygen desorption process. Study was conducted on other sorbent materials with improved separation capacity and chemical stability. The calcium-based sorbents are proven to be stable under CO_2 atmosphere at 800°C. Doping lanthanum and bismuth decreases the stability of the materials in CO_2 environment. However, with strontium doping, the desorption rate is significantly improved.

1. Perovsktie Sorbents with Oxygen Vacancy Order-Disorder Transtion

1.1 Materails studied

Our initial interest was in utilizing order-disorder phase transition to enhance oxygen sorption/desorption rate. Since oxygen is a more desirable product in most industrial process and the perovskite metal oxides only adsorb oxygen, the key to employ these materials practically are the desorption efficiency. Early research conducted by Yin et al. [1-3] showed that with disorder-to-order phase transition, the oxygen desorption rate was significantly enhanced. Since during the desorption process the phase of the perovskite oxide transforms from disordered phase to ordered phase, we define it as disorder-order transition, while order-disorder transition take place along with sorption process. Metal oxide sorbents with oxygen vacancy order-disorder transition are listed in Table 1. Among the these sorbents, LSCF1991 has highest oxygen adsorption capacity at 500-600°C and fastest oxygen desorption rate (all these sorbents have fast oxygen sorption rates). Thus, our initial effort was to focus on measurements and analysis of oxygen sorption and kinetic data on LSCF1991 sorbent.

Table 1. Characteristics of Metal Oxide Sorbents with Oxygen Vacancy Order-to-Disorder Transition

Sorbent	$SrCo_{0.8}Fe_{0.2}O_{3-\delta}$ (SCF82)	$La_{0.1}Sr_{0.9}Co_{0.9}Fe_{0.1}O_{3-\delta}$ (LSCF1991)	$SrCoFeO_{3-\delta}$ (SCF111)
Operation temperature (°C)	400-700	500-700	700-800
Apparent heat of adsorption (kJ/mol)	0-40	0-20	N/A
Oxygen sorption capacity (mmol/g)	400--0.48 500--0.34 600--0.32 700--0.23	500--0.55 600--0.45 700--0.37	600--0.29 700--0.27 800--0.42 900--0.41
Oxygen desorption rate (1/s)	$0.5\text{-}2x10^{-2}$	$0.2\text{-}1x10^{-2}$	$0.5\text{-}3x10^{-2}$

1.2. Oxygen Adsorption Isotherms and Isobars, and Desorption Kinetics for LSCF1991

Figures 1 and **2** show oxygen adsorption isotherms and isobars on LSCF1991 obtained in our lab. This adsorbent does not adsorb nitrogen. As shown in **Figure 1**, below 700°C where order-disorder transtion occurs with change of oxygen pressure, pressure swing may give higher adsorption capacity with a faster adsorption and desorption rate. It is important that the pressure swing is carried out in the pressure ranges that oxygen-vacancy order-disorder transition takes place.

Isobar data given in **Figure 2** are interesting. At oxygen partial pressures above 0.03 atm, increasing temperature lowers amount of oxygen adsorbed, so the conventional temperature swing

process may be used. However at pressures lower than 0.03 atm, increasing temperature may result in a jump in oxygen adsorption amount (at the transition point), followed by a decrease in oxygen adsorption amount with increasing temperature. The conventional thermal swing process would not work here.

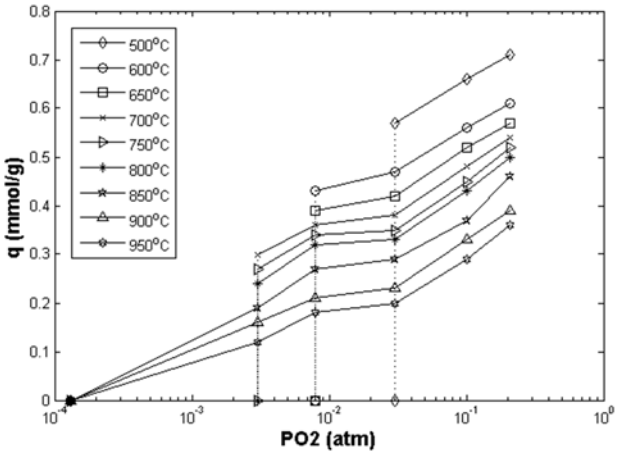

Figure 1. Oxygen sorption isotherms of LSCF1991

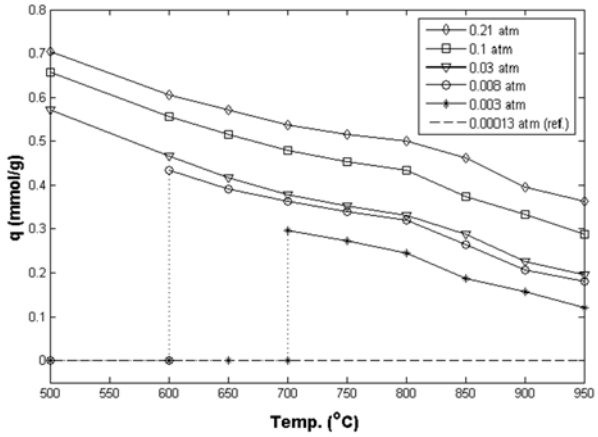

Figure 2. Oxygen sorption isobars of LSCF1991

Without order-disorder transition, the heat for oxygen adsorption in LSCF1991 is about

$$\Delta H_{sorp}=-185 \text{ kJ/mol}$$

the minus sign indicates exothermic heat in oxygen sorption, with "mol" means oxygen adsorbed. If there is order-to-disorder transition in oxygen sorption step, the endothermic heat of transition is:

$$\Delta H_{trans}=60 \text{ kJ/g}$$

So for a pressure swing process involving oxygen vacancy order-disorder transition, the modified heat for oxygen adsorption is:

$$\Delta H_{Modifed}=\Delta H_{trans}+ \Delta H_{trans} /q \quad (1)$$

where q is the amount of oxygen adsorption (in unit of mol/g not mmol/g), and $\Delta H_{Modifed}$ has unit of kJ/mol.

If we use the following liner driving force model to describe the sorption or desorption kinetic:

$$\frac{dq}{dt} = k(q_e - q) \qquad (2)$$

Integration gives:

$$\frac{q}{\Delta q} = [1 - \exp(-kt)] \quad (3)$$

sorption or desorption rate constant can be estimated from the half-weight change time $t_{1/2}$ (time at $q/\Delta q = 0.5$) from the transient uptake curves. Typical results are given in **Table 2**. The temperature for without-transition process is around 800ºC and that for with-transition process is 700ºC. As shown, the oxygen desorption rate is about 2 orders of magnitude lower than the oxygen adsorption rate when there is no oxygen order-disorder transition. In the case with the transition, the oxygen desorption rate is much higher and becomes the same as the oxygen sorption rate.

Table 2. Oxygen sorption and desorption rate constants on LSCF metal oxide sorbent

	Without transition	With transition
Adsorption k (1/s)	$1.4x10^{-2}$	$1.4x10^{-2}$
Desorption k (1/s)	$3.5x10^{-4}$	$1.4x10^{-2}$

1.3 Fixed-bed Experiments

We built a lab-scale fixed-bed experiment setup which comprises two mass flow controllers, a four-way valve and related pipe fittings, a tubular furnace, a dense alumina tube packed with silica grain and sorbent, and an oxygen analyzer. A simple layout of the setup is illustrated in **Figure 3**. Before it was used for the sorption/desorption experiment, the dead volume of the system was tested by using an alumina tube packed with only silica grain. The results show that the dead volume of the system is about 15 ml.

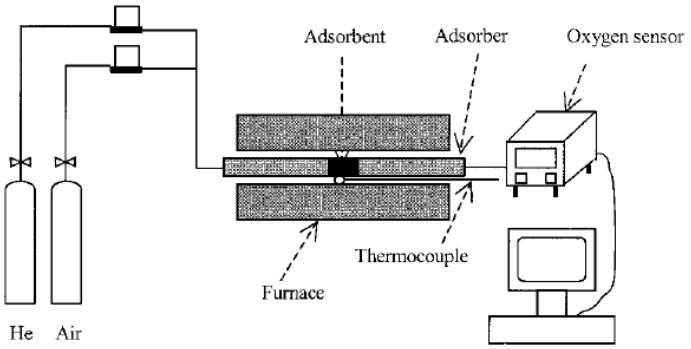

Figure 3. Fixed-bed setup layout

The operation conditions of the fixed-bed experiment were: both air and helium (purge) were set to be 5 ml/min under 1 atm, 2 grams of LSCF1991 powders are packed, the packing length is about 4 cm, and a thermocouple probe is in the middle of the packing. **Figure 4** shows the sorption breakthrough curves from 400-800°C. LSCF1991 TGA data and LSCF1964 fixed-bed data are also listed Table 3 and compared with LSCF1991 fixed-bed data. Except the fixed-bed sorption at 800°C, all other fixed-bed data are accordant with TGA data (the difference of the two results at 800°C are about 12%). The sorption capacity is in a trend that it increases with decreasing temperature.

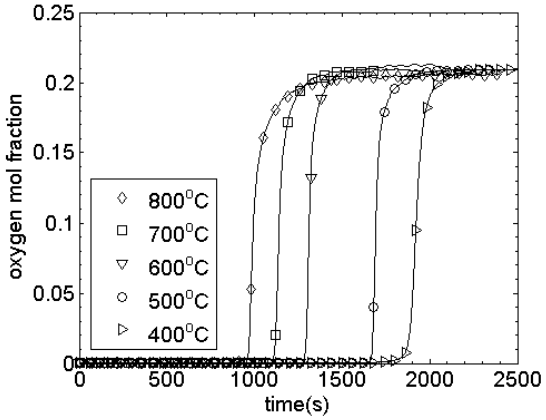

Figure 4. LSCF1991 sorption breakthrough curves.

Unlike the sorption capacity which varies with temperature, the desorption amount and efficiency does not change much with the temperature, as presented by **Figure 5** and **Table 4**. Although it is certainly lower at 800°C compared with other conditions, the results at 500°C to 700°C are very close. In the first hour of desorption, the desorption amount increase with

decreasing temperature.

Table 3. LSCF1991 and LSCF1964 sorption data comparison.

Temperature(°C)	Fixed-bed, LSCF1991 (mmol/g)	Fixed-bed, LSCF1964 (mmol/g)	TGA, LSCF1991 (mmol/g)
400	0.645	0.396	0.641
500	0.569	0.388	0.544
600	0.467	0.403	0.460
700	0.378	0.350	0.388
800	0.325	0.293	0.291

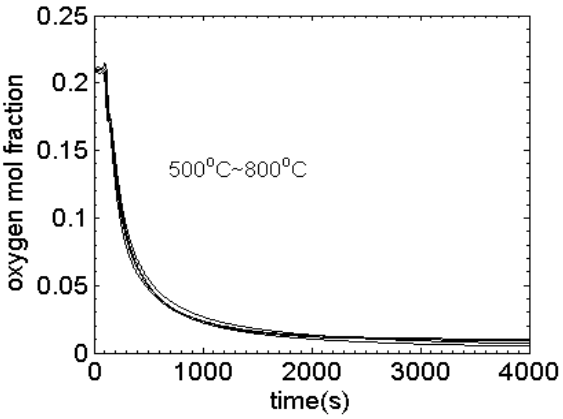

Figure 5. LSCF1991 desorption breakthrough curves. The results are very close.

Table 4. LSCF1991 desorption data

Temperature(°C)	1hr desorption amount(mmol/g)	1hr desorption efficiency	2hr desorption amount(mmol/g)	2hr desorption efficiency
500	0.167	29.3%	0.205	36.0%
600	0.162	34.2%	0.217	45.8%
700	0.161	42.6%	0.212	56.1%
800	0.142	43.7%	0.165	50.8%

The temperature change of LSCF1991 sorption/desorption processes were recorded by the

thermocouple. **Figure 6** shows the temperature change during the sorption process at different temperature. The temperature change is very accordant with DSC data [4]. Begin with from 400°C, the trend of heat released decreases as the temperature increases. To 700°C, there is only minimal heat effect. At 800°C, the process turn to endothermic, which is regarded as an evidence of phase transition.

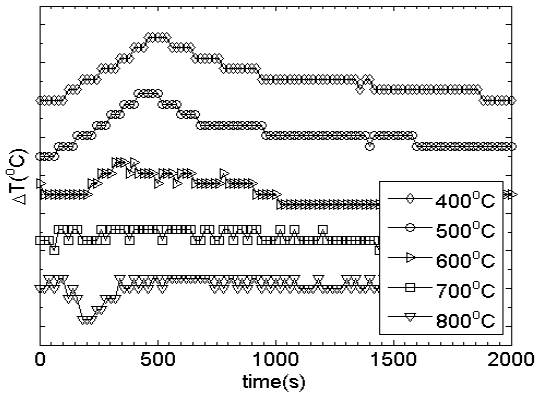

Figure 6. Temperature change during LSCF1991 sorption process.
Each single tick on y-axis represents 1°C

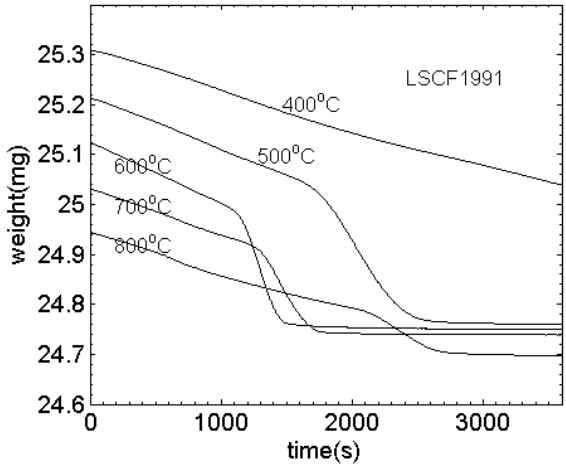

Figure 7. LSCF1991 TGA desorption curves.

The material of LSCF1991 has a unique property called order-disorder phase transition, as discussed earlier. From the desorption curves, as shown in **Figure 7**, we can tell from the sharp turn that phase transition happens at 500°C to 800°C . In addition, with phase transition, the process reach equilibrium much faster than one without phase transition (the curve of 400°C).

Moreover, the desorption rate is not in a monotonic trend with increasing or decreasing temperature. Begin with 400°C , it increases with increasing temperature. At 600°C it reaches maximum, then decreases with increasing temperature. If compared with fixed-bed results, the two data sets does not seem to agree with each other very well. Because of huge difference of the equipment and scale (2 g vs 20 mg), a simple correlation may not be found between these two data sets.

1.4 Desorption Rate Comparison

With order-disorder phase transition and sharp reduction of weight in TGA desorption data, it is expected that LSCF1991 has faster desorption rate than LSCF1964. However, the fixed-bed desorption data show unexpected results. After comparing the TGA data of the two materials in detail, the question can be explained. **Figure 8** shows the comparison of LSCF1991 and LSCF1964 TGA desorption data at each temperature. As can be seen from the figures, although there are no sharp turns in LSCF1964 weight curves, the initial slope is larger under most conditions, which explains why it has faster desorption rate. On the other hand, although after the presence of phase transition, the weight reduction of LSCF1991 is faster and also it does reach equilibrium state in a shorter time, the initial slope is smaller than LSCF1964 in many cases. The only exception is the result at 600ºC. At this temperature, LSCF1991 desorption is slightly faster than LSCF1964 in the whole time frame. Since the powder used in the fixed-bed were much more than in TGA, the scale of time from of these two characterization method might also differ significantly. It is possible that the phase transition of LSCF1991 does not happen at the time frame of fixed-bed desorption, therefore the desorption rate is slower as the slope of the curves indicate.

We hypothesized the key factor of the disorder-order phase transition could be (1) oxygen nonstoichiometry, since the oxygen vacancies would affect the lattice structure of the material, or (2) oxygen partial pressure around the sorbents, since it would affect the thermodynamic driving force for oxygen transport. **Figure 9 (a)** shows the oxygen nonstoichiometry curves of the desorption process. As the data indicate, the desorption rate increases at δ=0.33, 0.35 and 0.38 at 500, 600 and 700°C, respectively. It can be observed that the points at which desorption rate was enhanced are close to the boundary between disordered phase region and two-phase region, as **Figure 9 (b)** shows [2]. If phase transition will take place at the specific δ values of LSCF1991 in fixed-bed, then the phase transition should happen at the expected time listed in last column of

Table 5. However, as **Figure 5** presents, no obvious enhancement in the desorption rate can be observed.

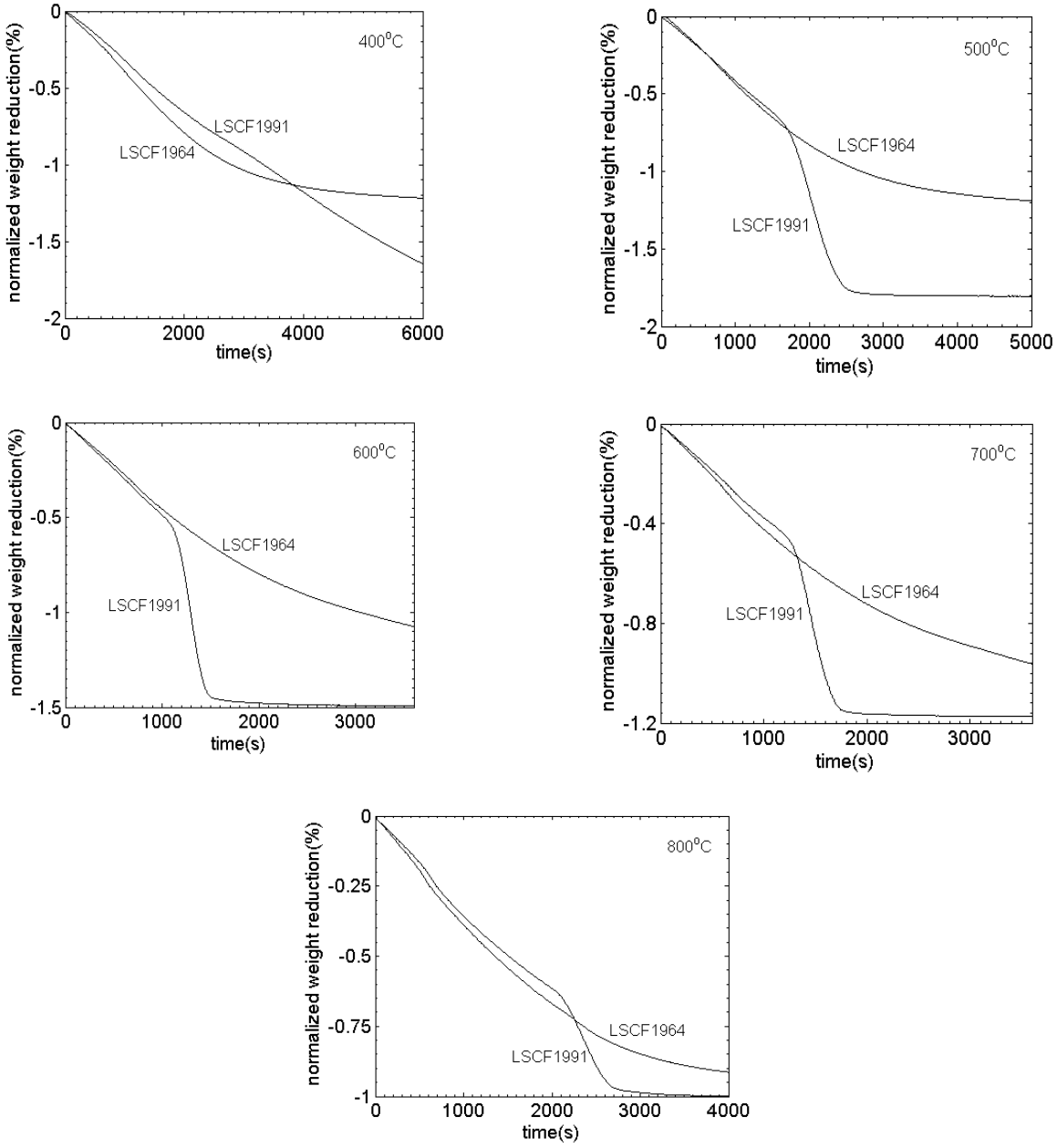

Figure 8. TGA desorption data comparison of LSCF1991 and LSCF1964.

Table 5. Estimated time to observe enhanced desorption rate in fixed-bed.

Temp. (°C)	δ when when rate increases	δ when equilibrium	Oxygen desorption percentage when rate increase	Corresponding fixed-bed desorption amount (mmol)	Expected time to observe enhanced rate in fixed-bed desorption (min)
500	0.323	0.475	32%	0.182	41.5
600	0.345	0.478	27%	0.126	12.6
700	0.375	0.481	28%	0.105	10.2
800	0.421	0.483	50%	0.143	27.0

Table 6. Comparison in experiment conditions and oxygen concentration in purge.

Experiment set-up		Sorbent amount	Purge flow rate	Initial oxygen desorption rate per unit mass (at 600°C)	Estimated P_{O2} in purge
TGA		20 mg	100 ml/min	5.309×10^{-5} mol O_2/min·g sorbent	3.595×10^{-4} atm
Fixed-bed		2 g	5 ml/min	2.335×10^{-5} mol O_2/min·g sorbent	0.193 atm

Figure 10 shows the XRD spectrum of the quenched sample. Fresh sample XRD spectrum at room temperature and in-situ high temperature XRD spectrum at 600°C are included as references of perovskite and brownmillerite phase, respectively. As seen from Figure 10, although there are some low-intensity peaks which does not match the in-situ high temperature spectrum, the quenched sample evidently transformed into a phase close to brownmillerite. Since the sample were quenched in fixed-bed after two hours of desorption, the sample may yet reach equilibrium and developed into well-defined brownmillerite phase. Therefore the peaks present at $2\theta=29.1°$ and 44.3°, which are absent at high temperature spectrum, may result from lower crystallinity of the quenched sample. In addition, it is noteworthy that the oxygen partial pressure in the high-temperature XRD vacuum chamber is much lower than in the fixed-bed at the moment when the samples were quenched. The XRD results suggest that even enhanced desorption rate was not observed, the phase transition still occurred during the fixed-bed desorption.

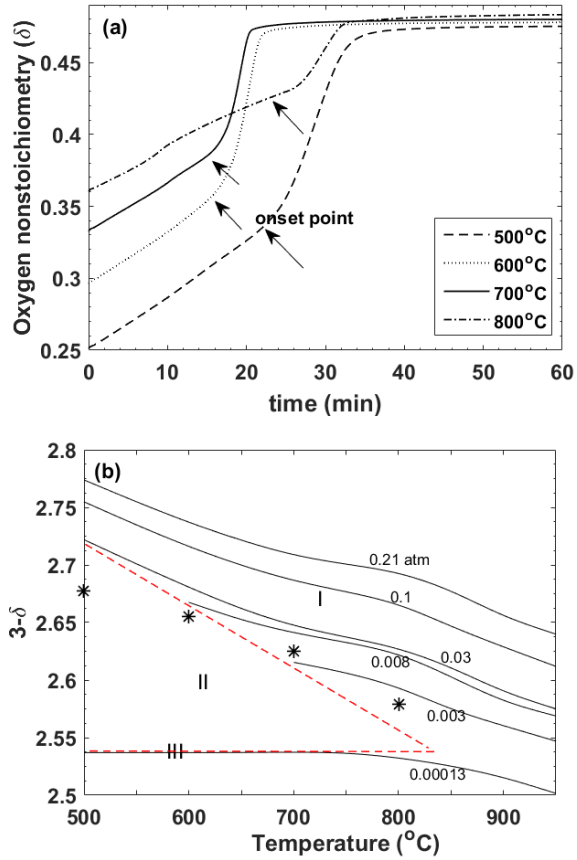

Figure 9 (a) LSCF1991 oxygen nonstoichiometry (δ) vs time during the desorption process at 500-800°C. The arrows indicate the onset point of phase transition. (b) Observed rate-enhanced points on LSCF1991 phase diagram (shown as *).

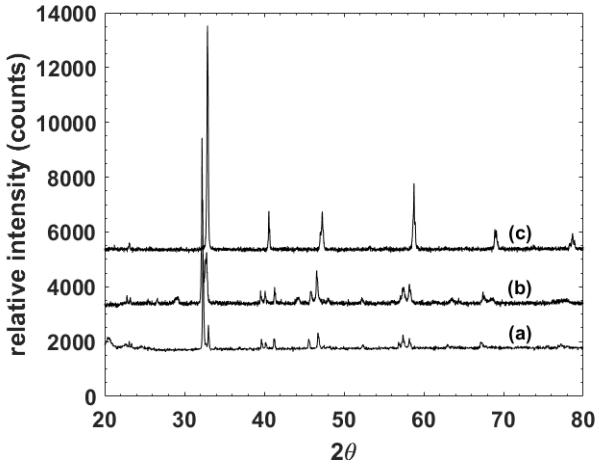

Figure 10. XRD spectrum of LSCF1991 of (a) in-situ high temperature scanning at 600°C (b) sample quenched from fixed-bed at 600°C and (c) fresh sample. The peak present in (a) at 2θ=20° resulted from the polymer vacuum dome of high temperature set-up.

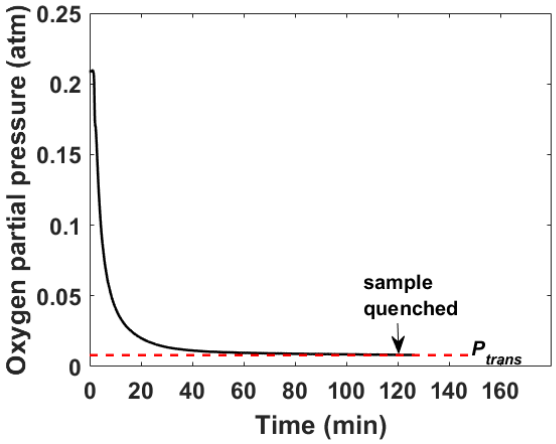

Figure 11. Comparison between oxygen partial pressure during LSCF1991 fixed-bed desorption at 600°C and oxygen partial pressure where phase transition takes place (P_{trans}).

The difference between the TGA and fixed-bed results implies that the disorder-order phase transition will not happen at the specific vacancy concentration (or δ value) if the working conditions are different. Based on the results we suppose that the oxygen partial pressure around the sample has major effect of the phase transition kinetics. Unlike TGA, in which oxygen partial pressure of the purge gas is assumed in the magnitude of 10^{-4} atm at any time, the oxygen partial pressure in fixed-bed surrounding the particles is much higher. A simple semi-quantitative comparison of the two experiments is presented in **Table 6**. The initial oxygen desorption rate (defined as the rate from the start to 95% weight reduction) at 600°C calculated from the TGA data is 5.309×10^{-5} mol O_2/min·g sorbent. Under such operation condition the estimated P_{O2} in the purge gas is 3.595×10^{-4} atm. On the other hand, the initial desorption rate of fixed-bed (calculated from desorption breakthrough curve, defined as the rate from the start to 95% weight reduction) is 1.572×10^{-5} mol O_2/min·g sorbent, which is 44.0% of the rate in TGA. The oxygen partial pressure surrounding the sorbents in the fixed-bed is as high as 0.193 atm, as estimated by time average of outlet concentration. Such high-P_{O2} environment might prevent the disorder-order phase transition from happening.

Despite the phase transition still take place as proven by the XRD results, the phase transition may only take place in the late stage of the fixed-bed desorption process. By referring to Figure 9 (b), for LSCF1991 desorption at 600°C, the P_{O2} at which the disorder-order phase

transition takes place is about 0.008 atm. Then as **Figure 11** illustrates, the oxygen concentration of effluent during the desorption process reached such value (indicated as P_{trans}) at about 100-120 min. The high P_{O2} in fixed-bed in the early stage of the desorption process may not provide enough driving force for the phase change, which explains why no enhanced desorption rate were observed.

Table 7. Nomenclature and properties of perovskite materials investigated in this work.

formula	abbreviation	structure (room temperature, $P_{O_2} = 0.21$atm)	phase transition temperature (°C , under $P_{O_2} = 10^{-4}$atm)	δ_0
$La_{0.1}Sr_{0.9}Co_{0.9}Fe_{0.1}O_{3-\delta}$	*LSCF1991*	peroveskite, cubic	846	0.168
$La_{0.1}Sr_{0.9}Co_{0.6}Fe_{0.4}O_{3-\delta}$	*LSCF1964*	perovskite, cubic	N/A	0.134
$La_{0.2}Sr_{0.8}Co_{0.6}Fe_{0.4}O_{3-\delta}$	*LSCF2864* ***(WRI sample)***	perovskite, cubic	N/A	0.212
$SrCo_{0.8}Fe_{0.2}O_{3-\delta}$	*SCF82*	perovskite, hexagonal	770	0.277
$SrCo_{0.5}Fe_{0.5}O_{3-\delta}$	*SCF55*	perovskite, cubic	795	0.201

2. Study on Other Perovskite Sorbents with Improved Properties

2.1. Expending La-Sr-Co-Fe materials

The selection of sorbents was expanded in order to discover a material with better sorption/desorption performance. The LSCF-series metal oxide investigated in this project are listed in **Table 7**. LSCF2864 were found in WRI inventory and showed decent fixed-bed sorption/desorption result.

In order to get some understanding of phase transition properties of WRI sample, temperature ramping test were done in TGA/DSC. Ramping were programmed in 5°C/min and with 100ml/min nitrogen purge (P_{O2}~10^{-4}). As shown in **Figure 12**, an endothermic peak presents in the ramping test data of LSCF1991, SCF55 and SCF82, respectively. And the temperature at the onset point were determined and listed in **Table 7** as phase transition temperature. The presence of endothermic peak indicates that these three materials have phase transition property. On the contrary, there are no peaks exist in the heat flow data of LSCF1964 and WRI sample, which

means that these two materials have no phase transition property and would be in perovskite phase during the whole sorption/desorption process.

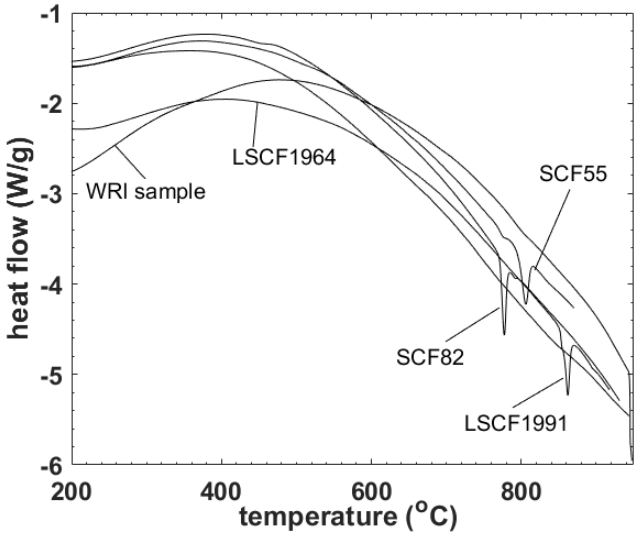

Figure 12. Temperature ramping test in nitrogen (P_{O2}~10^{-4}) of LSCF1964, WRI sample (without phase transition) and LSCF1991 (with phase transition)

Table 8. Sorption capacity of perovskite materials

Temp.(℃)	LSCF1964 (mmol/g)	LSCF1991 (mmol/g)	SCF82 (mmol/g)	SCF55 (mmol/g)	WRI sample (mmol/g)
900	--	0.256	--	--	0.283
800	0.300	0.291	0.265	0.252	0.296
700	0.366	0.388	0.244	0.323	0.328
600	0.405	0.460	0.285	0.398	0.345
500	0.418	0.544	0.361	0.492	0.354
400	0.379	0.641	0.461	0.596	--

The sorption/desorption properties of the five perovskite sorbents were tested in TGA. **Table 8** compares the sorption capacities of the materials have been studied. As the data indicated, almost all the materials follow the same trend that their sorption capacity decreases with increasing temperature. However, despite good desorption performance in fixed-bed, the sorption capacity at medium-low temperature of the WRI sample is rather low. At 500°C its sorption capacity is 35%

lower than of LSCF1991 and 15% lower than of LSCF1964. On the other hand, at higher temperature range, 700°C to 800°C, the sorption capacity of the three materials are compatible.

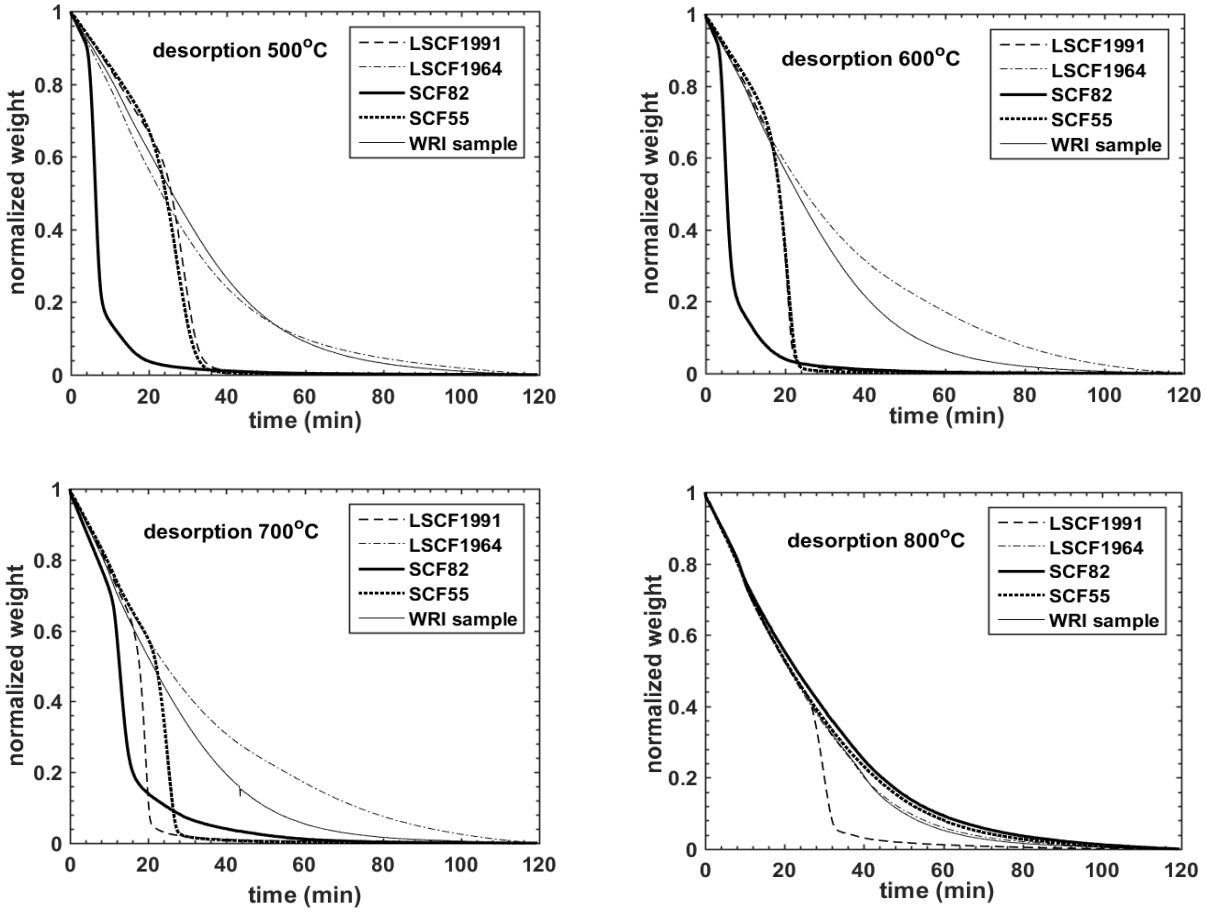

Figure 13. Desorption comparison at 500-800°C

Figure 13 present the weight change during the TGA desorption process at different temperatures. At 500°C, desorption rates of LSCF1964 and WRI sample are similar. While at 600°C and 700°C, desorption rate of WRI sample becomes faster after 30 minutes of the process. However, at 800°C, the two materials again have similar desorption rates. An interesting phenomenon is that except LSCF1991, which still has phase transition at 800ºC, all other materials have similar desorption rate at this temperature.

Figure 14 compare the desorption rate (1/s) of 10%, 50%, and 90% of weight reduction. WRI sample (circle) shows increasing initial rate as the temperature increases. However, the 50%

desorption rate and 90% desorption rate almost remain unchanged when changing temperature. In addition, WRI sample has very similar desorption rate with LSCF1964, which does not have phase transition property, at all stages. Sorbents with phase transition property have higher desorption rate at moderate temperature range. For example, the 50% desorption rate of SCF82 at 600°C is about 3 times as the rest, and the 90% desorption rate of LSCF1991 is about 2.7 times as of WRI sample

2.2. Development of CO_2-tolerant sorbents

Since the disorder-order phase transition may not bring significant breakthrough in promoting oxygen desorption efficiency due to operational constraint, our focus on material research switch to the development of CO_2-tolerant sorbents. The biggest challenge of LSCF perovskite oxide is the Sr ion at A-site of the perovskite structure tend to react with carbon dioxide at working temperatures (500-800°C). Similar problem were reported on barium-containing perovskite oxide as well. A strategy to increase CO_2 resistance is to reduce or completely replace the strontium content in the sorbent. Based on electronegativity trend, the larger elements, such as barium and strontium, have stronger tendency to donate electron and thus react with acid. On the other hand, the smaller IIA group elements, such as calcium and magnesium, are more stable because of lower electronegativity compared with the heavier elements.

Figure 15 shows the thermodynamic analysis of carbonation reaction of CaO, SrO and BaO. As the data indicate, the Gibbs free energy of calcium carbonation is less negative than the other strontium carbonation and barium carbonation, which suggest that calcium-rich perovskite oxide may be more resistant to carbon dioxide compared with strontium or barium rich materials. Therefore we decide to synthesize and test $CaMnO_{3-\delta}$ (CM) as the start of our material design. Modification of CM were also conducted in order to improve the oxygen sorption/desorption of this material.

Figure 16 shows the oxygen sorption isotherm data of CM along with previously investigated materials for comparison (note that CM isotherm is at 800°C, since CM can only work under this temperature). As indicated by the isotherm shape, CM is even more favorable in oxygen adsorption than other perovskite oxide, which might indicate it is unfavorable in oxygen desorption in PSA process in thermodynamic point of view.

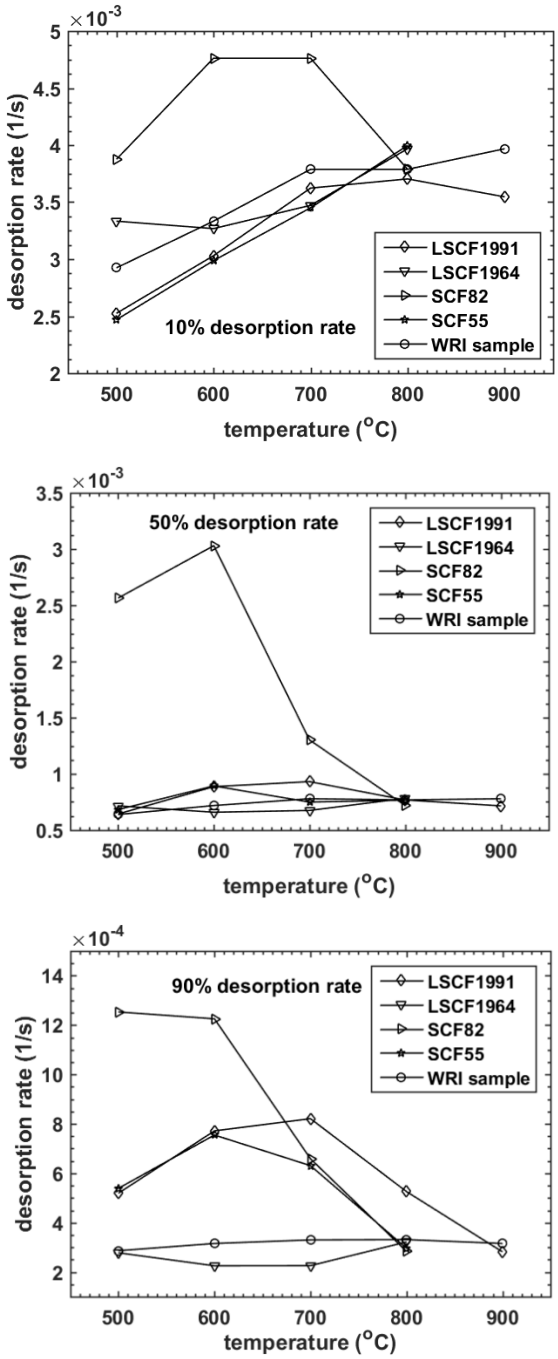

Figure 14. 10%, 50% and 90% desorption rate comparison.

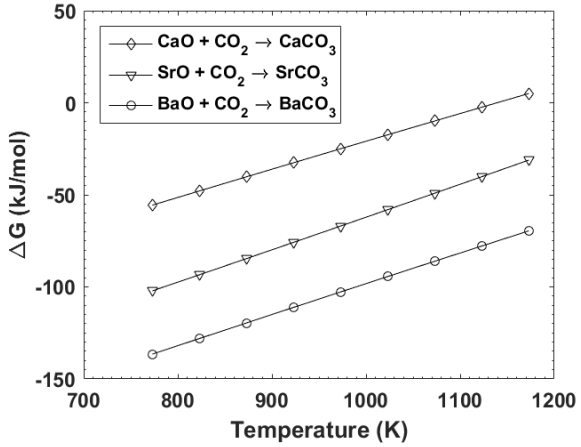

Figure 15. Gibbs free energy of the carbonation reaction of oxides of IIA group metals.

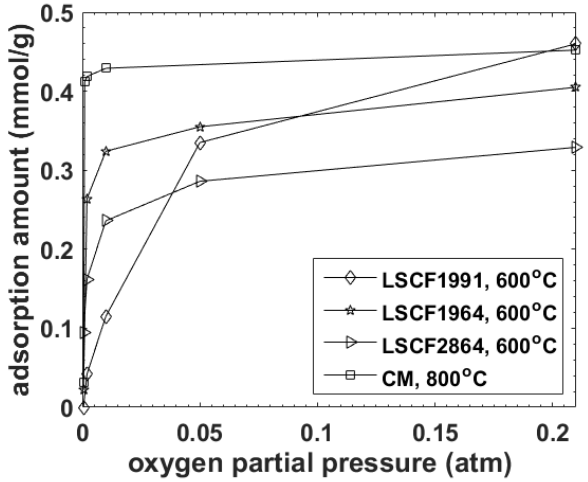

Figure 16. Oxygen sorption isotherm of CM compared with reference perovskite sorbents.

The fixed-bed experiment were conducted in the same set-up as the previous experiments. Two grams of powders were packed, and the diameter and length of the bed are about 50mm and 6mm, respectively. Oxygen (99.5% purity) and carbon dioxide were used as sorption and desorption gas. Both gas stream were fixed at the flow rate of 5ml/min (outlet stream). Due to fine particles there was pressure drop across the bed. The pressure of the inlet stream were 11psig in sorption and 12psig in desorption. The sorption and desorption breakthrough curves were obtained, as shown in **Figure 17** and **18**. The sorption capacity calculated from the sorption breakthrough curve under such pressure is 1.375 mmol/g. This value is as 3.2 times as the sorption capacity

tested in TGA under P_{O2}=0.21atm. The desorption capacity and efficiency data are listed in **Table 9**. LSCF2864 (WRI sample) fixed-bed desorption data are listed in **Table 10** for comparison.

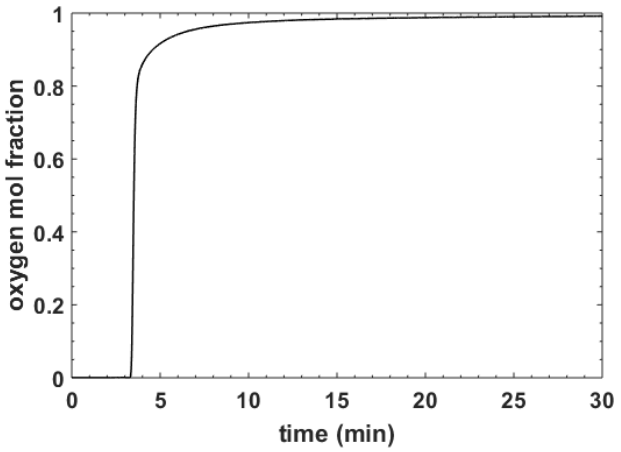

Figure 17. Oxygen sorption breakthrough curve of CM at 800°C and 11psig feed pressure.

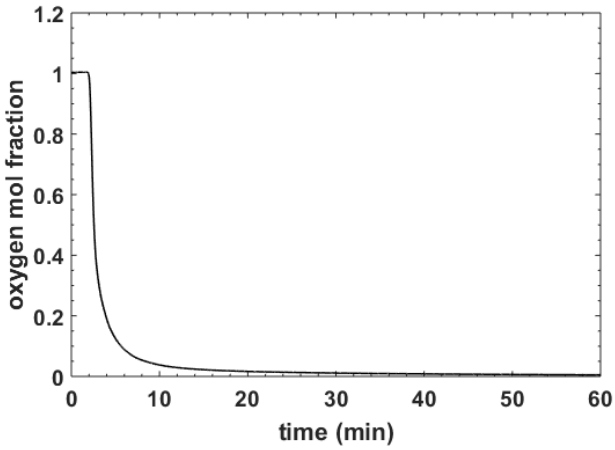

Figure 18. Desorption breakthrough curve of CM at 800°C and 12 psig purge pressure.

Table 9. Desorption performance data of CM at 800°C and 12 psig purge pressure.

Desorption capacity 30min (mmol/g)	Desorption efficiency 30min (%)	Desorption capacity 1hr (mmol/g)	Desorption efficiency 1hr (%)
0.877	63.8	0.900	65.5

As the data indicated, operating the CM fixed-bed at higher pressure does promote the sorption capacity while maintaining decent desorption efficiency. To demonstrate the capability of producing oxygen-rich gas stream, sorption/desorption cycle in fixed-bed were conducted. **Figure 19** shows the cyclic sorption/desorption process data with 3 min of cycle time and **Figure 20** shows the data with 1.5min of cycle time. The sorption periods are represented by the O_2 marks in the figure, while the CO_2 marks represent the desorption periods. The oxygen concentration of outlet stream fluctuated between 0.08-0.93 with 3min of cycle time. On the other hand, with 1.5 min of cycle time the outlet oxygen concentration is in the range of 0.20-0.86, which is more desirable compared with the previous result.

Table 10. Desorption data of LSCF2864 (WRI sample) at various temperatures.

Temperature	Desorption capacity 30min (mmol/g)	Desorption efficiency 30min (%)	Desorption capacity 1hr (mmol/g)	Desorption efficiency 1hr (%)
500	0.158	48.5	0.191	48.5
600	0.168	53.1	0.204	53.1
700	0.167	62.7	0.202	62.7
800	0.162	65.5	0.194	65.5

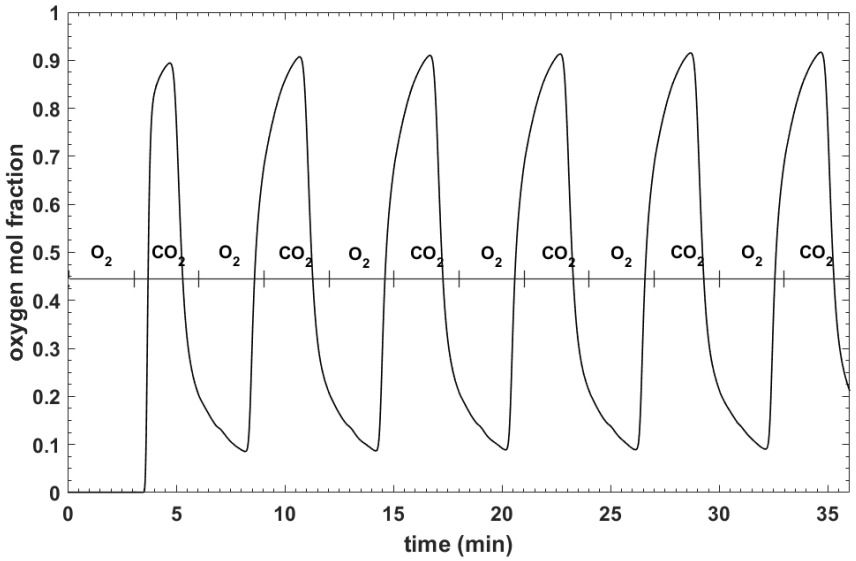

Figure 19. Fixed-bed sorption/desorption cycle of CM at 800°C with 3min of cycle time.

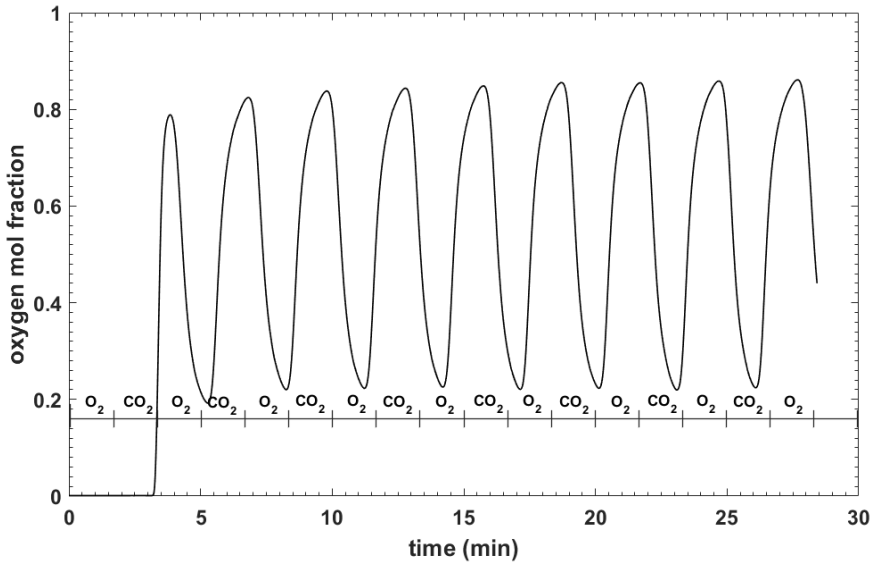

Figure 20. Fixed-bed sorption/desorption cycle of CM at 800°C with 1.5min of cycle time.

M-O bond	Bond dissociation energy (kJ/mol, 298K)
Bi-O	343
Co-O	368
Mn-O	402
Fe-O	409
Sr-O	454
Ca-O	464
Ba-O	563
Sm-O	619
Nd-O	703
Ce-O	795
La-O	799

Table 11. M-O bond dissociation energy at 298K of candidate metal ions.

Element	Ionic radius (pm)		
	2+	3+	4+
Ca	114		
Sr	132		
Bi		117	
La		117.2	
Sm	136	109.8	
Ce		101	87
Nd	143	112.3	
Co (hs*)	88.5	75	67
Co (ls**)		79	68.5
Fe (hs)	92	78.5	
Fe (ls)	75	69	72.5
Mn	67	58	53

Table 12. Ionic sizes of candidate metal ions
*ls: low-spin electron spin state
**hs: high-spin electron spin state

Based on the above results we tried to modify this material by doping other metal ions to promote its performance. The main goal is to enhance either the sorption capacity or desorption

rate. In order to increase the vacancy concentration and desorption rate, the candidate metal ions should be of 3+ or higher positive charge [6], in similar size with Ca^{2+} and have low M-O bond dissociation energy. **Table 11** lists the M-O bond dissociation energy of common metal ions. As the comparison shows, Bi-O has the lowest dissociation energy among all the candidates. In addition, **Table 12** [7] shows that the ionic sizes of Bi^{3+}, La^{3+}, Sm^{3+}, Nd^{3+} are similar to Ca^{2+}. Based on these readily information, the aforementioned metal ions are chosen as dopants for modifying CM for better oxygen sorption/desorption performance. **Table 13** [8] lists formability and the sorption/desorption characteristics in air/N_2 of the compositions have been synthesized. All materials were synthesized by liquid citric method.

Table 13. Phase formability and O_2 sorption behavior of synthesized sorbent.

Composition	**Forms single phase**	**Considerable O2 sorption capacity**	**Note**
$CaMnO_3$	Yes	Yes	Considerable sorption capacity at 800°C, stable in CO_2 environment.
$Bi_{0.1}Ca_{0.9}MnO_3$	Yes	Yes	Considerable sorption capacity at 800°C, not stable at CO_2 environment.
$La_{0.1}Ca_{0.9}MnO_3$	Yes	Yes	Considerable sorption capacity at 800°C.
$La_{0.5}Ca_{0.5}MnO_3$	Yes	No	
$Y_{0.1}Ca_{0.9}MnO_3$	Yes	Yes	Undesirable desorption rate.
$Y_{0.5}Ca_{0.5}MnO_3$	No	--	
$Sr_{0.1}Ca_{0.1}MnO_3$	Yes	Yes	Considerable sorption capacity at 800°C.
$Nd_{0.2}Ca_{0.8}MnO_3$	Yes	No	
$Nd_{0.5}Ca_{0.5}MnO_3$	Yes	No	
$Sm_{0.76}Ca_{0.24}FeO_3$	No	--	
$Sm_{0.5}Ca_{0.5}MnO_3$	No	--	
$SmCo_{0.1}Fe_{0.9}O_3$	No	--	

$SmCo_{0.3}Fe_{0.7}O_3$	No	--	
$SmCo_{0.5}Fe_{0.5}O_3$	No	--	
$SmCo_{0.8}Fe_{0.2}O_3$	No	--	

As **Table 13** presents, only $Bi_{0.1}Ca_{0.9}MnO_3$ (BCM19), $La_{0.1}Ca_{0.9}MnO_3$ (LCM19) and $Sr_{0.1}Ca_{0.1}MnO_3$ (SCM19) have the values that warrant further research. Since the doping amount of all these three composition are rather low (10% at A-site), the structure of the material should not change much. As **Figure 21** shows, the XRD spectrum of all these three modified materials are still in the same structure with CM (orthorhombic perovskite).

The oxygen sorption/desorption properties were tested in TGA in two different conditions: N_2/air switching and CO_2/O_2 switching (both are in 800°C). The oxygen sorption capacities of these materials measured in both conditions are CM: 0.452, BCM19: 0.244, LCM19: 0.176, SCM19: 0.438, all in mmol/g. As the data indicate, doping higher valence ions does not necessarily increase the sorption capacity. CM still has the highest sorption capacity among the four, while SCM19 slightly falls behind. **Figure 22** and **23** present the sorption and desorption rate of the sorbents in N_2/air test. Among the four sorbents, SCM19 has slightly slower sorption rate and faster desorption rate, while LCM19 has almost the same sorption rate and slower desorption rate. The results are in agreement with the M-O bond dissociation energy. As the bond energy is higher, the oxygen desorption rate should be lower. However, the result of BCM19 does not follow the rule. As seen from the figures, although it has slower sorption rate, its desorption rate is also the lowest among the four. At this stage the reason for this unexpected result is still unclear.

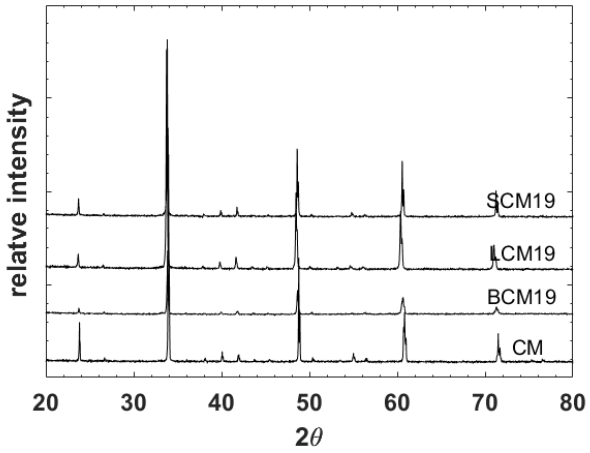

Figure 21. XRD spectrums of synthesized sorbents.

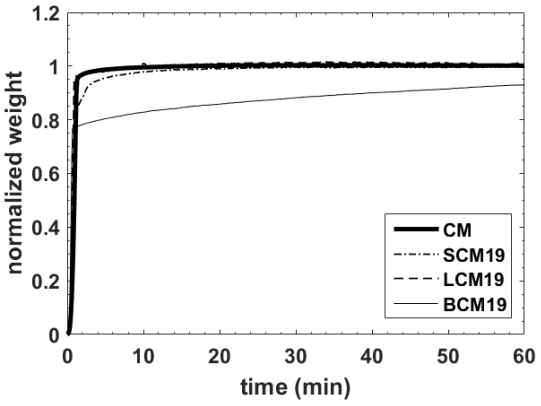

Figure 22. Normalized oxygen sorption curves in air/N2 of synthesized sorbents.

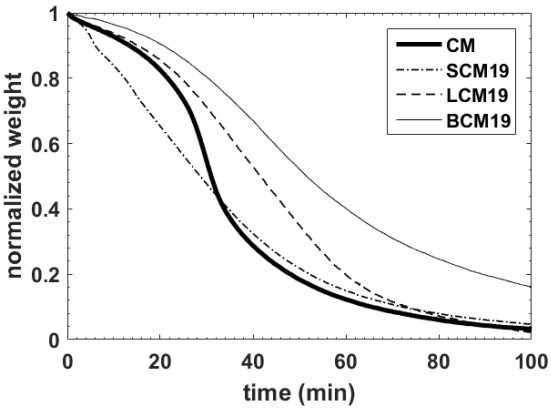

Figure 23. Normalized oxygen sorption curves in air/N2 of synthesized sorbents.

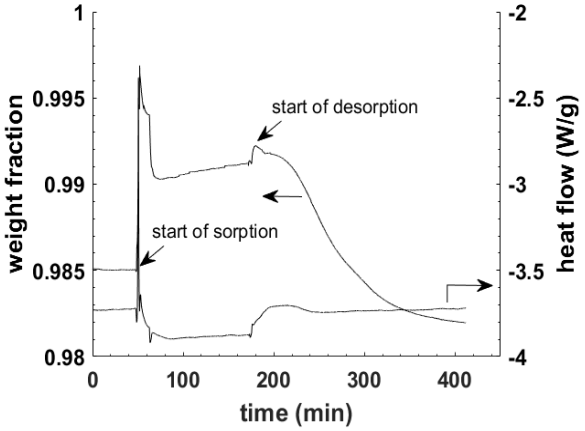

Figure 24. BCM19 sorption/desorption cycle at 800°C in CO_2/O_2 condition.

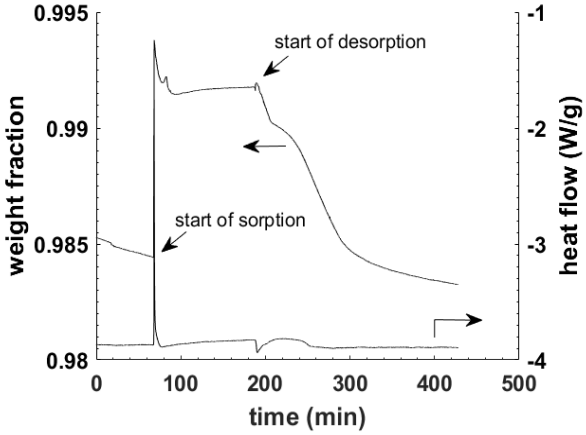

Figure 25. LCM19 sorption/desorption cycle at 800°C in CO_2/O_2 condition.

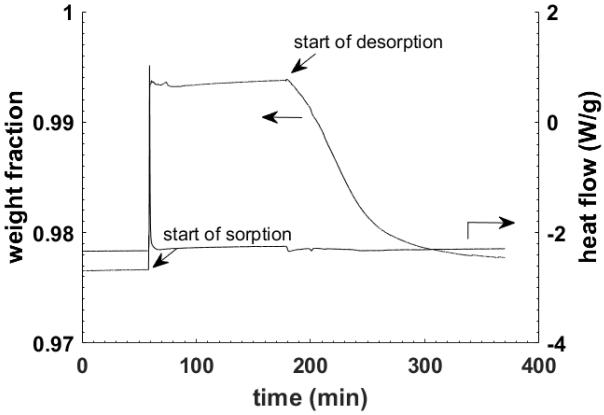

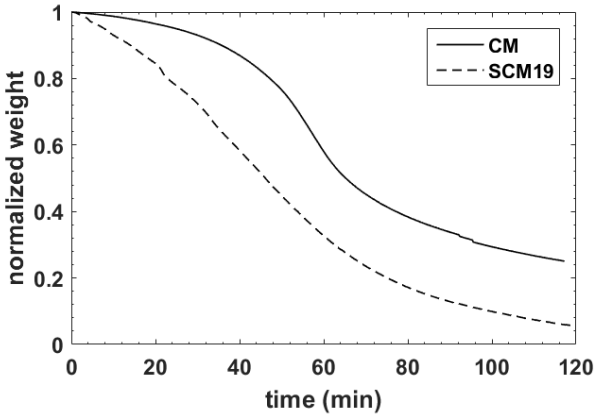

Figure 26. SCM19 sorption/desorption cycle at 800°C in CO_2/O_2 condition.

Figure 27. Normalized desorption curves of CM and SCM19 at 800°C in CO_2/O_2 condition.

In order to explore if the sorbents are suitable for CO_2-cycling oxy-fuel combustion process, CO_2/O_2 cycling tests were also conducted. However, LCM19 and BCM19 are not stable in CO_2. As **Figure 24** and **Figure 25** show, when switching from CO_2 to oxygen (start of sorption), the weight increases with a bump then drops down to a certain value, which suggest other chemical reactions might happen. On the contrary, SCM19 has better stability than the two sorbents mentioned before. **Figure 26** presents the sorption/desorption cycle of SCM19 in CO_2/O_2 switching condition at 800°C. As the figure shows there is no bump during the sorption process, and the weight can reach equilibrium before sorption and after desorption. Compared with CM at the same condition, the desorption rate of SCM19 is considerably faster, as shown in **Figure 27**.

3. Conclusions

TGA measurements show that the perovskite materials with the unique disorder-to-order phase transition property exhibit an oxygen desorption rate significantly faster than the materials without disorder-order phase transition. However, the disorder-order enhanced desorption rate is not observed in the fixed-bed desorption process. The oxygen partial pressure surrounding the sorbents is found to significantly affect the phase transition property. Due to high-P_{O2} in fixed-bed desorption process, the phase transition only happens in the late stage of desorption during the fixed-bed oxygen desorption process. The calcium-based sorbents are proven to be stable under CO_2 atmosphere at 800°C. Doping lanthanum and bismuth decreases the stability of the materials in CO_2 environment. However, with strontium doping, the desorption rate is significantly improved.

4. References

1. Q. Yin, Y.S. Lin. Beneficial effect of order–disorder phase transition on oxygen sorption properties of perovskite-type oxides. *Solid State Ionic*. **2007**, 178, 83–89

2. Q. Yin, J. Kniep, Y.S. Lin. High temperature air separation by perovskite-type oxide sorbents-heat effect minimization. *Chem. Eng. Sci.* **2008**, 63, 5870–5875

3. Q. Yin, J. Kniep, Y.S. Lin. Oxygen sorption and desorption properties of Sr–Co–Fe oxide. *Chem. Eng. Sci*. **2008**, 63, 2211-2218

4. Z.H. Yang, Y.S. Lin. Synergetic thermal effects for oxygen sorption and order–disorder transition on perovskite-type oxides. *Solid State Ionic*. **2005**, 176, 89–96

5. A. Yana, V. Maragoua, A. Aricod, M. Cheng, P. Tsiakaras. Investigation of a $Ba_{0.5}Sr_{0.5}Co_{0.8}Fe_{0.2}O_{3-\delta}$ based cathode SOFC: II. The effect of CO_2 on the chemical stability. *Appl. Catal., B.* **2007**, 76, 3-4,320-327

5. J. Sunarso, S. Baumann, J.M. Serra, W.A. Meulenberg, S. Liu, Y.S. Lin, J.C. Diniz da Costa. Mixed Ionic–Electronic Conducting (MIEC) ceramic-based membranes for oxygen separation, *J. Membr. Sci.* 320, **2008**, 13–41.

6. T. L. Cottrell. The Strengths of Chemical Bonds, 2d ed., Butterworth, London, **1958**

7. R. D. Shannon. Revised effective ionic radii and systematic studies of interatomic distances in halides and chalcogenides. Acta Crystallogr A. 32, **1976**, 751–767

Appendix II
ASU Subcontract Report

Professor Shuguang Deng

Final Report

"Sorbent-Based Oxygen Production for Energy Systems"

Federal Grant Number: DE-FE0024075

For Reporting Period of November 1, 2014 to September 30, 2016

Mai Xu, Shuguang Deng

Arizona State University
shuguang.deng@asu.edu

1. Introduction

There has been a growing interest on oxygen-enriched gas because of its multiple applications, such as steel, glass, and power generation. So far, a cryogenic air distillation method has been widely used as a commercial production process of oxygen, but it requires a large-scale plant as well as high energy cost. A sorbent-based oxygen production technique has been considered to be an attractive alternate for efficient oxygen separation from air at high temperatures.

The process utilizes perovskite-type oxides with a unique oxygen-storage property for air separation and oxygen removal. The oxygen content varies depending on oxygen partial pressure. Oxygen is stored in the oxide lattice during the sorption step, and release into a sweep gas such as CO2 or steam for gasification systems or recycled flue gas for oxy-combustion systems during the desorption step. This concept is based on a technology termed CAR (ceramic autothermal recovery) developed by the BOC group [1]. The cost of producing oxygen by using CAR was estimated to be 20-30% lower than using cryogenic air separation [1].

Pressure swing adsorption (PSA) technique has been considered to be one of the practical processes for the sorbent-based air separation. Some porous materials like activated carbons and zeolites, have been conventionally used as a nitrogen adsorbents for the PSA process operating at ordinary temperature [2-4]. Similarly, Lin and coworkers [5-9] suggested the repeatable oxygen adsorption/desorption cycles on perovskite-type oxides can also be performed by using PSA process at a high temperature. Previous studies has proven that the main features of this new type sorbents include infinitely large oxygen selectivity, relatively high-sorption capacity and high sorption rate [5].

On the other hand, simulation of PSA processes has been a great interest for researchers recently to avoid the need to build and run a pilot plant for design and optimization work. The mathematical modelling of PSA processes has been designed by a number of researchers [10-13]. But most of these papers are describing the PSA process on zeolite adsorbents operating at ordinary temperature. It is preferable if the high temperature PSA process on perovskite-type sorbents can also be modeled.

In the present work, the sorbent powder samples were provided by Dr. Lin's research group in Arizona State University. The sorbent powder were mixed with a binder and then compressed to a rod-shape pellet using a pellet press. The mechanical properties of the sorbent pellets were tested and compared with some commercial zeolite pellets. The breakthrough experiments by sorption of oxygen on the pellet samples were performed in a fixed bed. Simulations have been done for the sorbent-based air separation process in Matlab as well as ProSim DAC, a simulation software for dynamic adsorption column. The simulated results have been validated with the experimental data. The effect of pressure, cycle time and flow rate on oxygen purity were studied.

2. Experimental

2.1 Preparation of adsorbent pellets

The ceramic sorbent pellets LSCF-1991 were prepared with a pellet press with a 3 mm die set. The sorbent powder was firstly ground in an agate mortar before feeding to the die set. A propylene carbonate emulsion was also added as a binder. After pelleting, the pellets were sintered in the furnace at 1000 °C for 2 hours to strengthen their mechanical properties.

2.2 Mechanical properties

The mechanical properties of LSCF 1991 pellets were determined by testing their crush strength and attrition resistance. The crush strength of the pellets was tested by Instron Universal Mechanical Property Testing System. An increasing axial compressive load was forced on the sample until the sample deformed or fractured. The attrition and abrasion resistance of the pellets were tested using a standard test method ASTM D4058. The attrition testing units include a cylindrical drum with a single baffle, a motor and a standard sieve. The pellets were rotated for 30 minutes at a rate of 60 rpm in the drum. Fines produced by attrition and abrasion in the test were determined by sieving through the standard sieve.

Figure 1. Testing equipment for mechanical property of the pellets

The pellet sorbents were sintered at different temperatures from 500 °C to 1000 °C to study the relationship between sintering temperature and mechanical properties. The testing result is shown in Figure 2. It is found that higher sintering temperature helps to enhance the mechanical properties of the pellets, including both crush strength and attrition resistance. The temperature effect on the improvement of mechanical properties are more obvious when the sintering temperature is above 800 °C. Therefore higher sintering temperatures at 900 °C or 1000 °C are preferred. For the pellet samples sintering at 1000 °C, the crush strength limit can reach 596.39 N, while the attrition rate was 23.06 %. As a reference, the same tests were performed for some commercial zeolite pellets. The average crush strength for the zeolite samples was 77 N, and the average attrition rate was 2.3%.

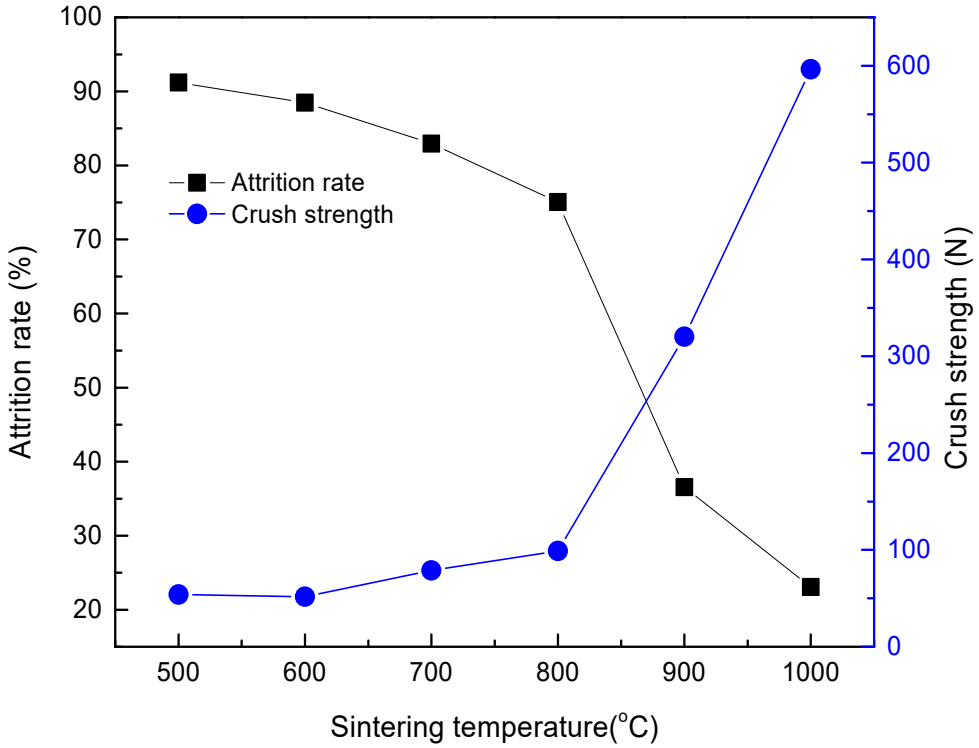

Figure 2. Mechanical properties of LSCF-1991 pellets at different sintering temperatures

2.3 Fixed-bed breakthrough experiment

For modeling a PSA process, the dynamic behavior of a packed adsorbent bed needs to be studied first. The overall pattern of the dynamic behavior is generally determined by the adsorption equilibrium, and may be strongly modified by kinetic effects. This dynamic behavior can be represented by a breakthrough curve, which is the outlet product concentration profile.

The air separation experiments by sorption of oxygen on LSCF 1991 pellets were performed in a fixed bed. The fixed-bed setup included an adsorber column, a heat insulation tube, a gas delivery system, an oxygen analyzer, and a data record system. Oxygen concentration of the exhaust gas was measured by the oxygen analyzer, so the sorption and desorption breakthrough data were recorded, which help to analyze the fixed-bed adsorption behavior. The adsorber column is an alumina tube of 0.5 inch i.d., the mass of adsorbent is 10 grams. Air at 1 atm was used as the feeding gas for sorption step, and nitrogen was used as purge gas for desorption step. Flow rate of air and nitrogen were both 30 ml/min.

Figure 3 and Figure 4 show the breakthrough curves for oxygen on LSCF-1991 pellets at different temperatures and flow rates. The shape of the curves at different temperatures and flow rates are quite similar. The breakthrough point can be achieved earlier when increasing the temperature or increasing the flow rates, because of the increasing temperature decreases saturation amount of oxygen and the increasing flow rates increases the rate of adsorption, which both decrease the breakthrough time.

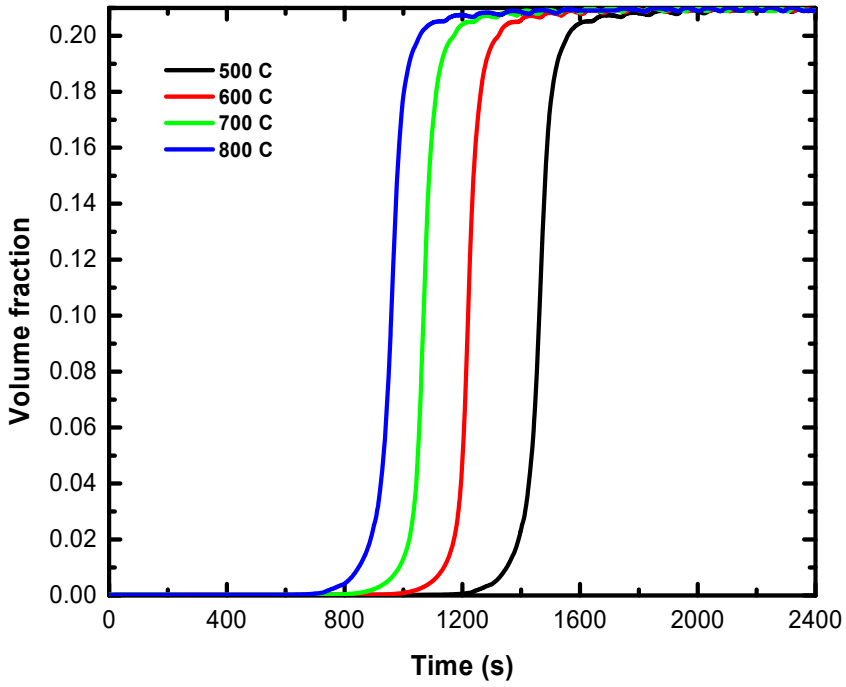

Figure 3. Breakthrough curves for oxygen on LSCF-1991 pellets at 500 ºC, 600 ºC, 700 ºC, and 800 ºC

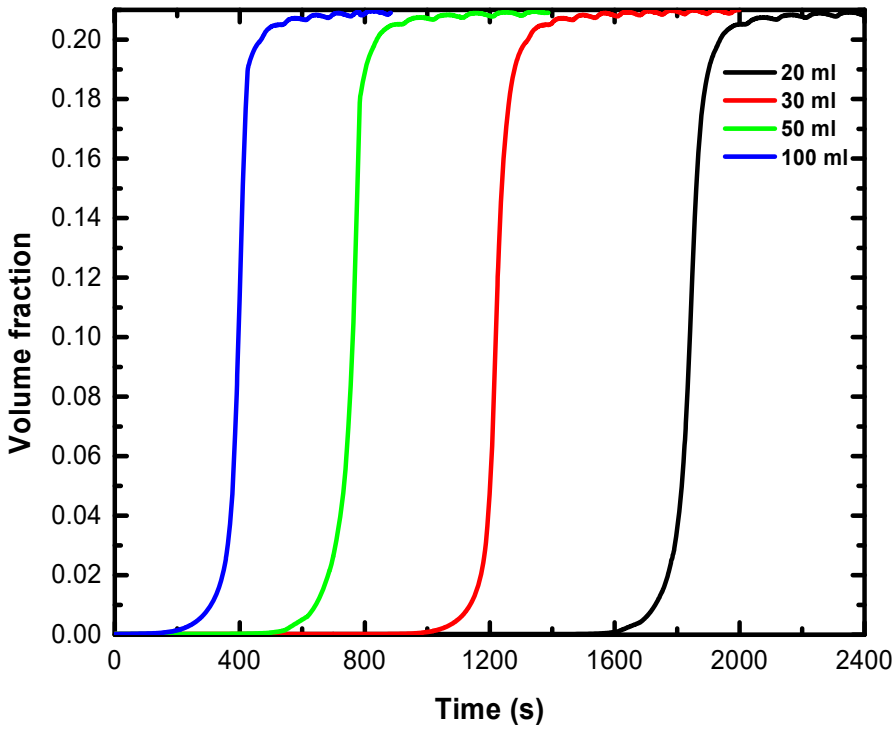

Figure 4. Breakthrough curves for oxygen on LSCF-1991 pellets at 600 ºC, flow rate = 20, 30, 50, and 100 ml/min

3. Dynamic simulation of adsorption column

A numerical simulation for the sorbent-based air separation using perovskite-type oxides was developed in Matlab. The simulation code was adapted from a thesis from Lehigh University [14]. The simulated result was validated with experimental data and compared with another dynamic adsorption simulation software, ProSim DAC. The simulation model was further used for PSA simulation and optimization.

3.1 Mathematical model of adsorption

Modeling of PSA process involves several partial differential equations (PDEs) in time and space. An initial condition and periodic boundary conditions were applied to link each processing step.

The equations describing the overall PSA cyclic operations are as follows. These PDEs can be solved by using inbuilt function ode15s in Matlab.

Gas phase mass balance for component i:

$$\varepsilon \frac{\partial (y_i \rho_g)}{\partial t} - \varepsilon D_L \frac{\partial^2 (y_i \rho_g)}{\partial z^2} + \frac{\partial (Q y_i)}{\partial z} + \rho_p \cdot \frac{\partial q_i}{\partial t} = 0$$

Gas phase overall mass balance:

$$\varepsilon \frac{\partial \rho_g}{\partial t} + \frac{\partial Q}{\partial z} + \rho_p \cdot \frac{\partial q_i}{\partial t} = 0$$

Solid phase mass balance for component i (mass transfer rates):

$$\frac{\partial q_i}{\partial t} = K_{pi}(q_i^* - q_i)$$

Mass transfer coefficient:

$$K_{pi} = \frac{60 D_{si}}{d_p^2}$$

The surface diffusion coefficient can be expressed with the following equation:

$$D_{si} = D_{so,i} \exp(\frac{-E_{si}}{RT})$$

The activation energy may be linked to the physical adsorption energy, with the following relation:

$$E_{si} = 0.45 \Delta H_{ads}$$

The pre-exponential factor may be assessed with the following expression:

$$D_{so,i} = \frac{1.61 \times 10^6}{\tau_s}$$

Langmuir adsorption equilibrium:

$$q_i = \frac{\left[q_{m0} \cdot \exp(\frac{q_{m1}}{T})\right]\left[K_o \cdot \exp(\frac{K_1}{T})\right] P_i}{1 + \left[K_o \cdot \exp(\frac{K_1}{T})\right] P_i}$$

The isotherm coefficients of the equation was estimated by correlating the experimental data. Figure 5 compared the experimental data and simulated curve for LSCF-1991 at 600 ºC. It's found that the isotherm model fits the experimental data quite well.

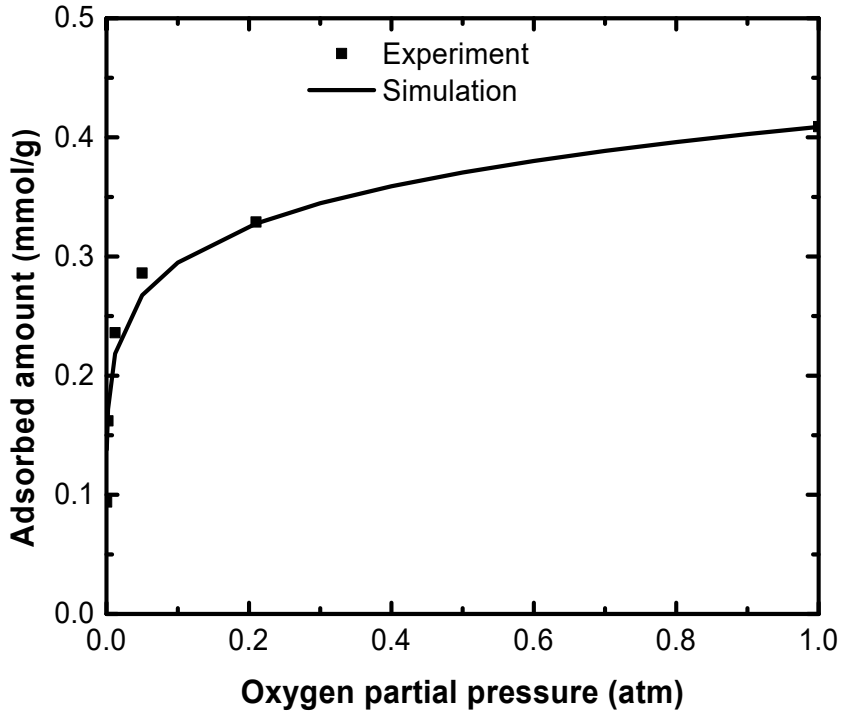

Figure 5. Experimental and simulated adsorption isotherm for oxygen on adsorbent at 600 ºC

Simulations of pressurization and depressurization steps were developed by a method using both Ergun equation and mass conservation equation. The equation can be further modified by coupling Darcy equation [1]. The equations describing the pressurization and depressurization steps are as follows.

For a gas which is not adsorbed,

$$\left(\frac{\partial P}{\partial t}\right)_z = -\frac{K}{\mu\varepsilon} \times \left\{\frac{\partial}{\partial z}\left[P(\frac{\partial P}{\partial z})_t\right]\right\}$$

For an absorbable gas,

$$\left(\frac{\partial P}{\partial t}\right)_z = -\frac{K}{\mu((1-\varepsilon)\rho f'(p)+\varepsilon)} \times \left\{\frac{\partial}{\partial z}\left[P(\frac{\partial P}{\partial z})_t\right]\right\}$$

where K is bed permeability, f'(p) is the gradient of adsorption isotherm with respect to pressure.

The initial and boundary conditions for the set of PDEs are described below, where component 1 is O_2 and component 2 is N_2.

Initial conditions:

$$y_1(z,0) = 0;\ \ y_2(z,0) = 1$$
$$\mathrm{P(z,0)} = P_0;$$

For adsorption and pressurization steps:

$$y_1(0,t) = 0.21;\ \ y_2(0,t) = 0.79$$
$$\mathrm{P(0,t)} = P_f$$

For desorption and depressurization steps:

$$y_1(L,t) = 0;\ \ y_2(L,t) = 1$$
$$\mathrm{P(L,t)} = P_p$$

Moreover, the final concentration and pressure of each step will equal with the initial concentration and pressure of next step.

3.2 Model parameters

Two sets of breakthrough simulations have been done in current work. One set is for sorbent powder, another set is for sorbent pellets. The equilibrium behavior of powder and pellets should be similar. The Langmuir isotherm parameters are presented in Table 1. The other model parameters, including sorbent properties, bed properties and feeding properties are summarized in Table 2 and Table 3.

Table 1. Adsorption isotherm parameters and heat of adsorption of O_2 on LSCF-1991

Parameters	Oxygen on LSCF-1991
q_{m0} (mol/kg)	0.1895
K_o (atm^{-1})	2.534
q_{m1} (K)	925
K_1 (K)	2865
Heat of adsorption (kJ/mol)	-30

Table 2. Model parameters of LSCF-1991 powder

Characteristics	Values
Sorbent particle size, d_p (mm)	0.1
Sorbent particle density, ρ_p (g/cm^3)	5.72
Sorbent heat capacity, C_p (J/kg/K)	1300
Packing length, L (cm)	5
Bed inside diameter, D (cm)	0.6
Bed voidage, ε	0.32
Flow rate of feeding gas (air), V_f (ml/min)	5
Feeding pressure, P_f (atm)	1
Flow rate of purging gas (N_2), V_p (ml/min)	5
Purging pressure, P_p (atm)	1

Table 3. Model parameters of LSCF-1991 pellets

Characteristics	Values
Sorbent particle size, d_p (mm)	2
Sorbent particle density, ρ_p (g/cm^3)	5.72
Sorbent heat capacity, C_p (J/kg/K)	1300
Packing length, L (cm)	5
Bed inside diameter, D (cm)	1.27
Bed voidage, ε	0.32
Flow rate of feeding gas (air), V_f (ml/min)	30
Feeding pressure, P_f (atm)	1
Flow rate of purging gas (N_2), V_p (ml/min)	30
Purging pressure, P_p (atm)	1

The PSA process of oxygen sorption on LSCF-1991 pellets was also simulated, the conditions were based on the experimental data from Western Research Institute (WRI), which presented in Table 4.

Table 4. Model parameters of PSA operations on LSCF-1991 pellets

Characteristics	Values
Sorbent particle size, d_p (mm)	1
Sorbent particle density, ρ_p (g/cm^3)	5.72
Sorbent heat capacity, C_p (J/kg/K)	1300
Bed length, L (inch)	12
Bed inside diameter, D (inch)	1
Bed voidage, ε	0.32
Flow rate of feeding gas (air), V_f (L/min)	2.8
Feeding pressure, P_f (psia)	20
Flow rate of purging gas (N_2), V_p (L/min)	0.55
Purging pressure, P_p (psia)	2
Adsorption time (s)	295
Desorption time (s)	295
Pressurization time (s)	5
Depressurization time (s)	5

3.3 Breakthrough curves and simulated curves

In order to validate the simulation results, several simulated breakthrough curves were compared with the experimental result for LSCF-1991 powder and pellets at 500 °C and 600 °C, which is shown from Figure 6 to Figure 9. It is observed that for all the figures, the two simulated breakthrough curves from Matlab and ProSim are almost overlapped with each other, and both of them are pretty close to the experimental breakthrough curve. It proves that the Matlab code can do a very similar simulation work with ProSim.

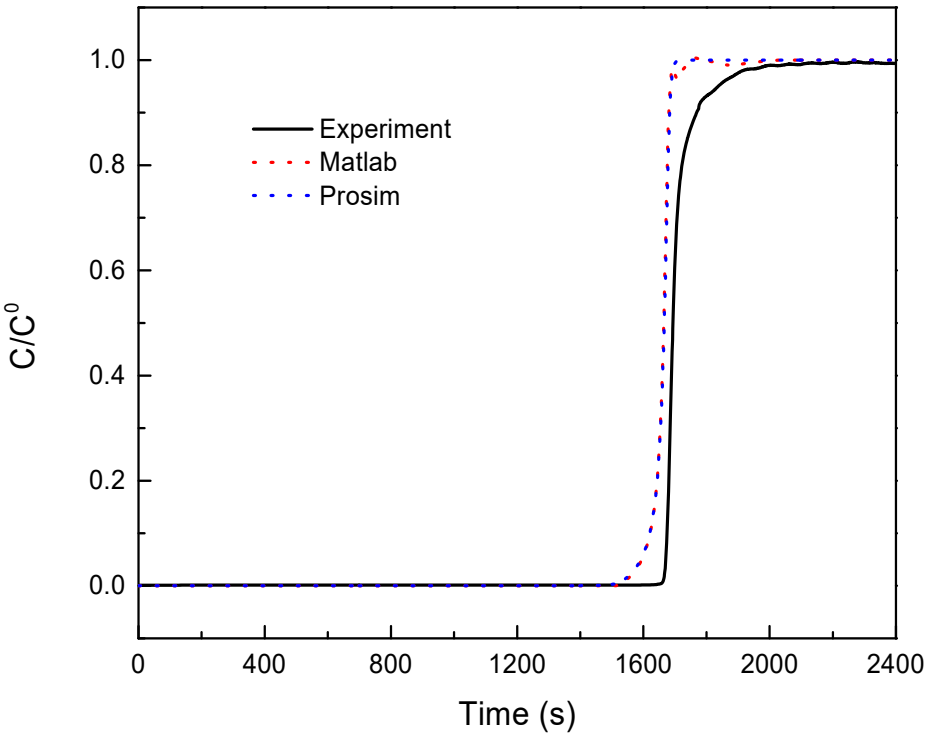

Figure 6. Experimental and simulated breakthrough curves for LSCF-1991 powder at 500 ºC

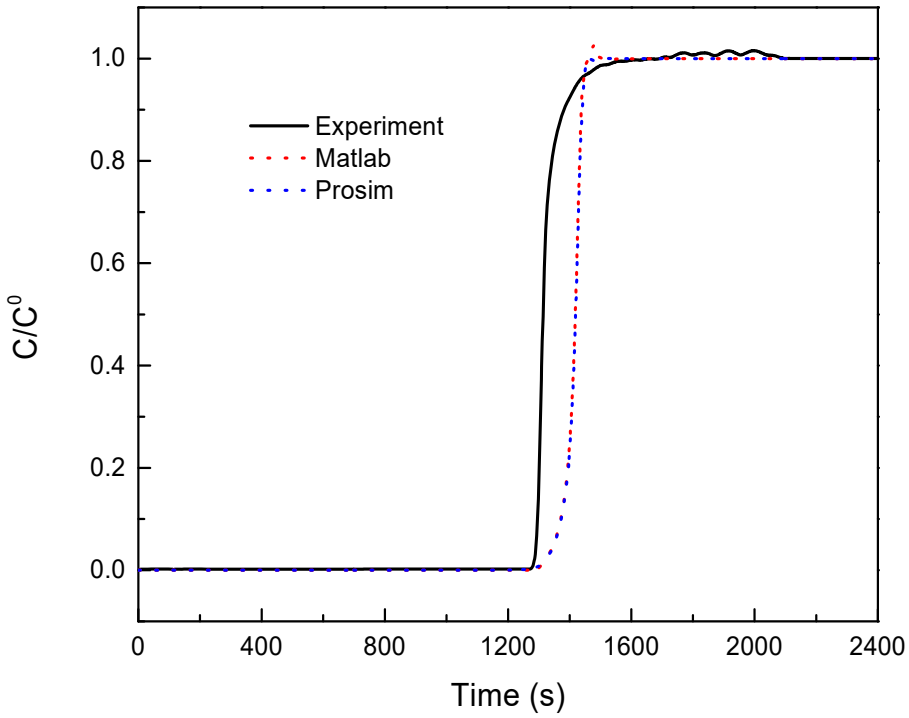

Figure 7. Experimental and simulated breakthrough curves for LSCF-1991 powder at 600 ºC

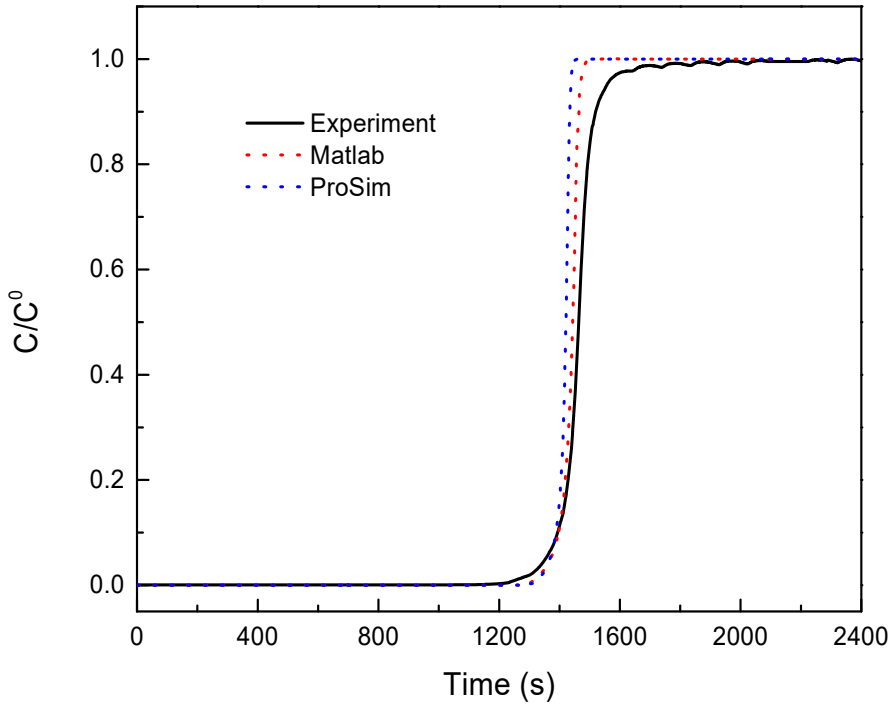

Figure 8. Experimental and simulated breakthrough curves for LSCF-1991 pellets at 500 ºC

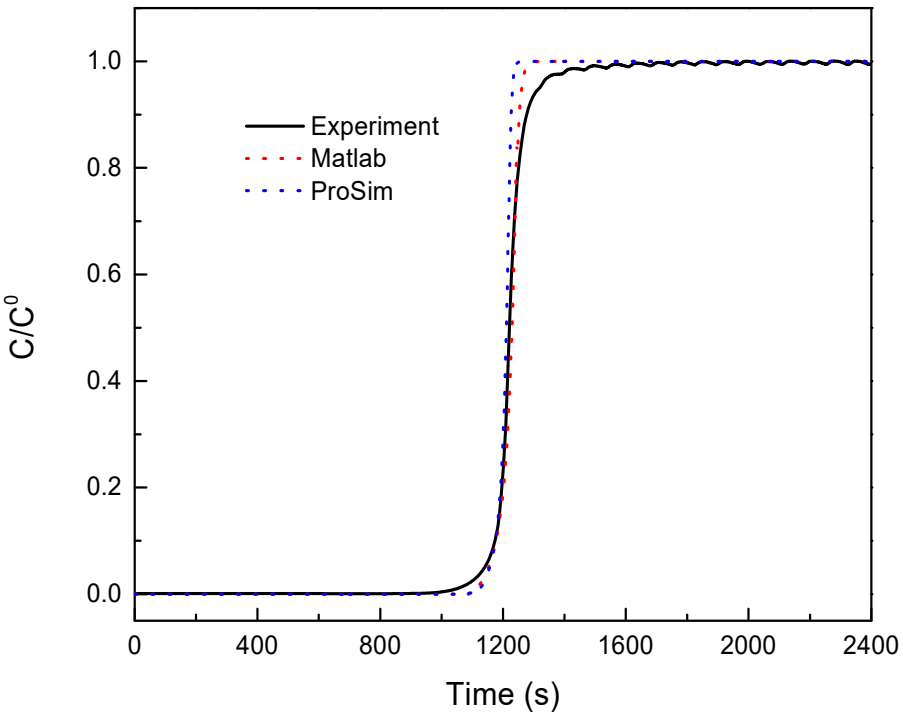

Figure 9. Experimental and simulated breakthrough curves for LSCF-1991 pellets at 600 ºC

3.4 3-D profiles in the fixed bed

Matlab is also able to make some 3-D plots to study the profiles of some variables changing with both time and column length, like 3-D profile of oxygen adsorbed amount in Figure 10, and 3-D profile of oxygen mole fraction in Figure 11. It's very clear to see how the adsorbed amount profile and oxygen fraction profile inside the column gradually moves from the inlet to the outlet of the column with the time going. Finally, the bed is saturated with oxygen, both adsorbed amount and oxygen mole fraction achieve a highest value and show no difference with the length of column. Figure 12 shows a contour plot of oxygen mole fraction made by Matlab modeling. It might be easier to tell how the profile change with time because it's a 2-D plot. Initially, the oxygen fraction is zero at all column position. After feeding air, oxygen started to appear at the inlet and the oxygen wave gradually from the inlet to the outlet. Finally, oxygen fraction goes to identical again at 0.21, which is the mole fraction of feed gas.

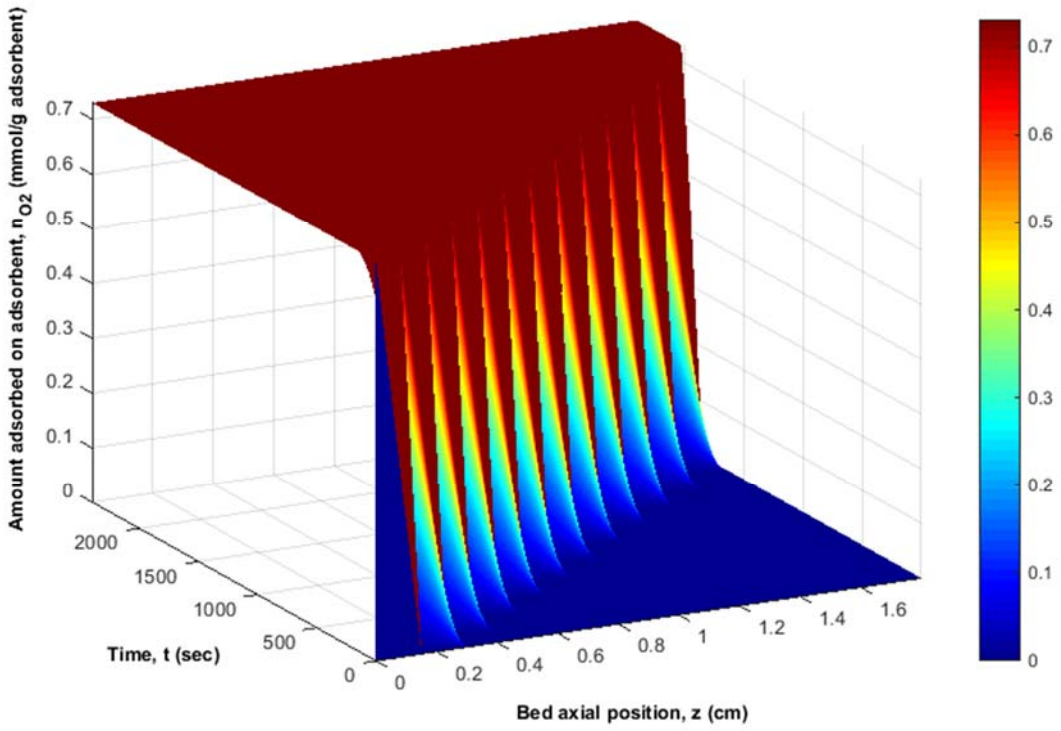

Figure 10. 3-D profile of oxygen adsorbed amount

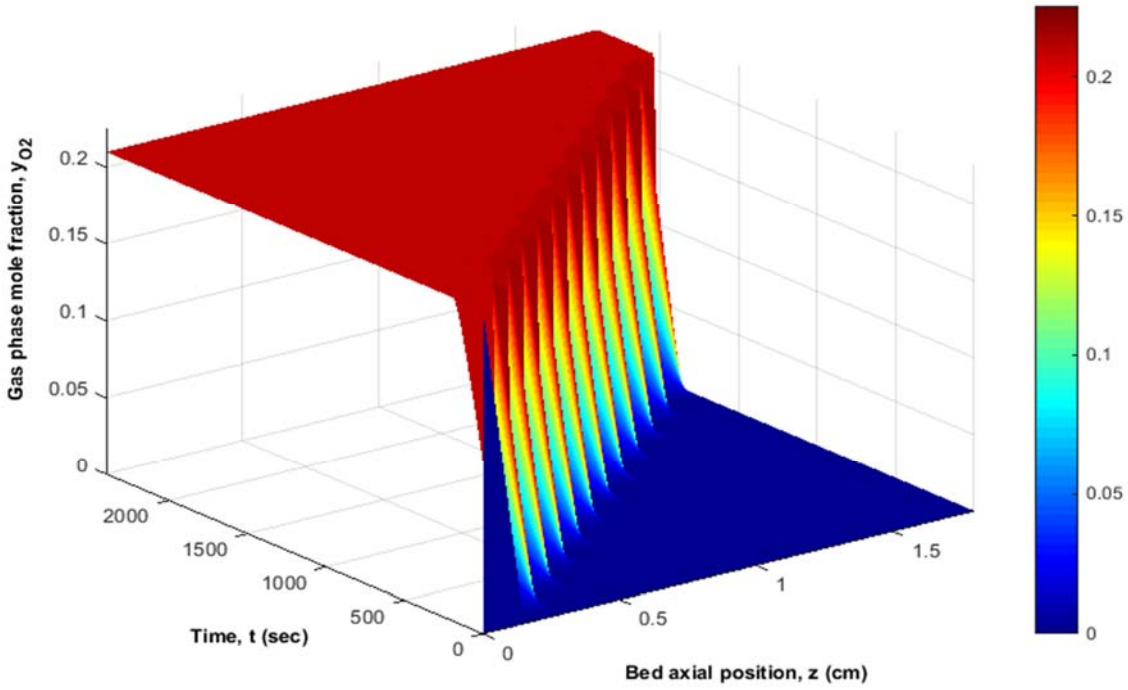

Figure 11. 3-D profile of oxygen mole fraction

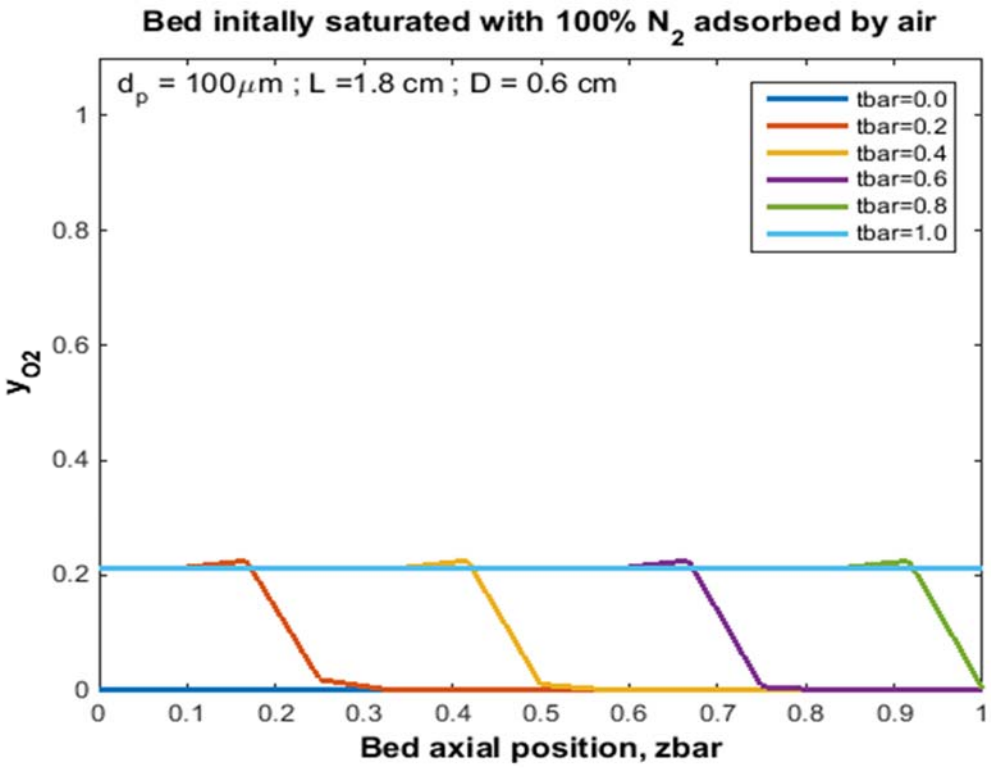

Figure 12. Contour plot of oxygen mole fraction

3.5 Oxygen profile of PSA simulation

For PSA simulation, several simulations were performed by Matlab based on WRI's experimental condition, which displayed in Table 4. The simulated oxygen concentration curve is shown in Figure 13. For each cycle, oxygen mole fraction increased to 0.21 during adsorption, just like how it behaved at the breakthrough curve. Further, there is a sharp increase at the beginning of purge step, as oxygen started to be recovered from the adsorbent pellets. After that, oxygen concentration decreased because the desorption rate slowed down. It is noticed that the concentration profiles for the cycles are similar, which indicates the bed reached to a cyclic steady state (CSS).

For numerical calculation, the adsorption bed was actually divided into several bed sections to discretize the PDEs. Figure 14 shows the variation of oxygen concentration along the time for different bed sections during a single PSA cycle at CSS. It is observed that all the curves had a similar shape, except the straight line, which meant the inlet concentration curve. Moreover, it can be clearly seen how oxygen flowed and being adsorbed through the bed, until the bed was totally saturated, and how oxygen released from the sorbent during purge step.

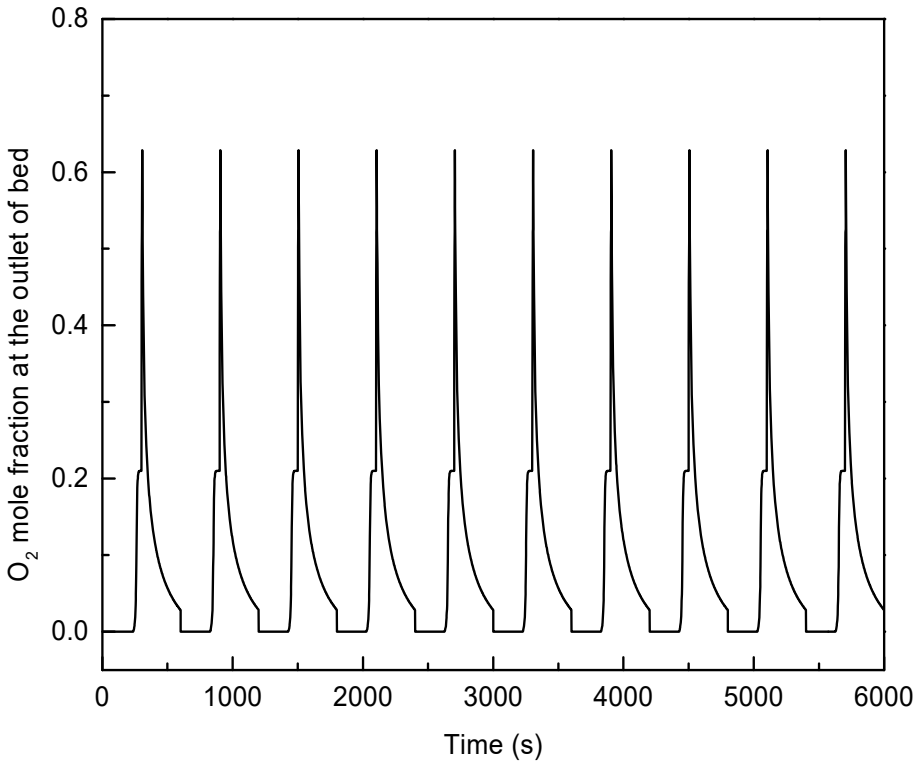

Figure 13. Oxygen mole percentage at the outlet of adsorption bed

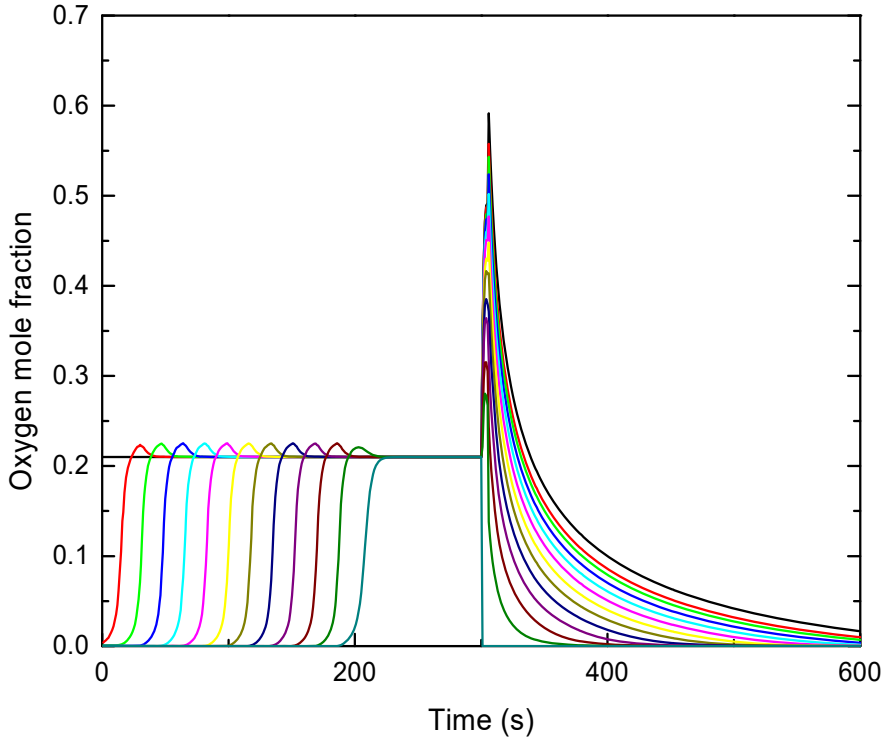

Figure 14. Oxygen mole fraction of one PSA cycle

3.6 Effects of model parameters of PSA

For the sorbent-based air separation process, the oxygen-enriched gas was produced by recovering the adsorbed oxygen from the adsorbent during desorption step. Usually the product gas of desorption step was collected in a storage tank. It is important to analyze the purity of oxygen in the tank. The oxygen purity can be calculated by using the following expression:

$$\text{Oxygen purity} = \frac{\int_0^{t_{desorption}} y_{O_2} dt}{t_{desorption}}$$

In order to increase the oxygen purity, several effects on product purity were studied based on the simulation package, including adsorption pressure, cycle time, duration of each step, and flow rates of purge gas.

The effect of adsorption pressure was investigated as shown in Figure 15, while keeping other parameters constant. It is found that oxygen purity increases when increasing the adsorption pressure increases. Because larger amount of oxygen is adsorbed at a higher pressure during adsorption, it is reasonable that larger amount of oxygen will be released as well during desorption. However, there is no significant increase above an adsorption pressure of 40 psia. Considering the

higher energy cost for the higher pressure, it is better to maintain the adsorption pressure around 40 psia.

Since desorption is a crucial step for the PSA operations on perovskite-type sorbents. The effect of desorption duration was studied while keeping the total cycle time constant. The pressurization and depressurization time were also kept constant. As shown in Figure 16, oxygen purity increased while reducing the duration of desorption. Therefore, to obtain a high oxygen purity in the product, it is recommended to have a short duration for desorption step.

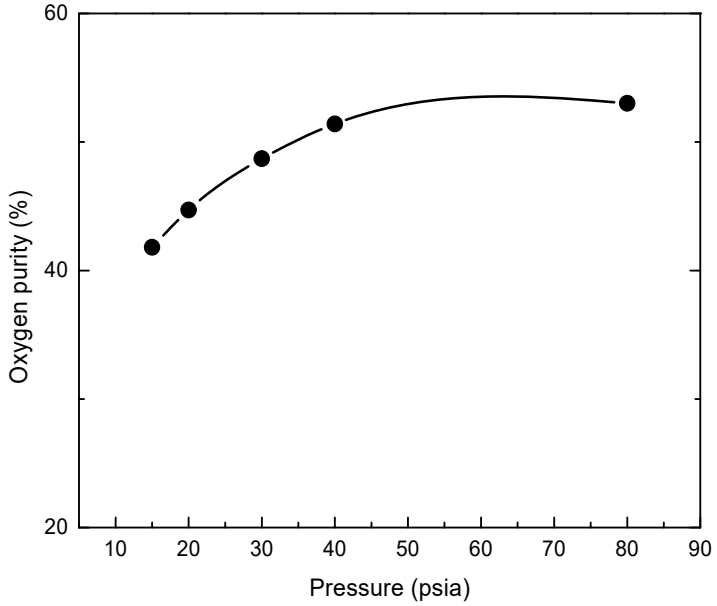

Figure 15. The effect of adsorption pressure on oxygen purity

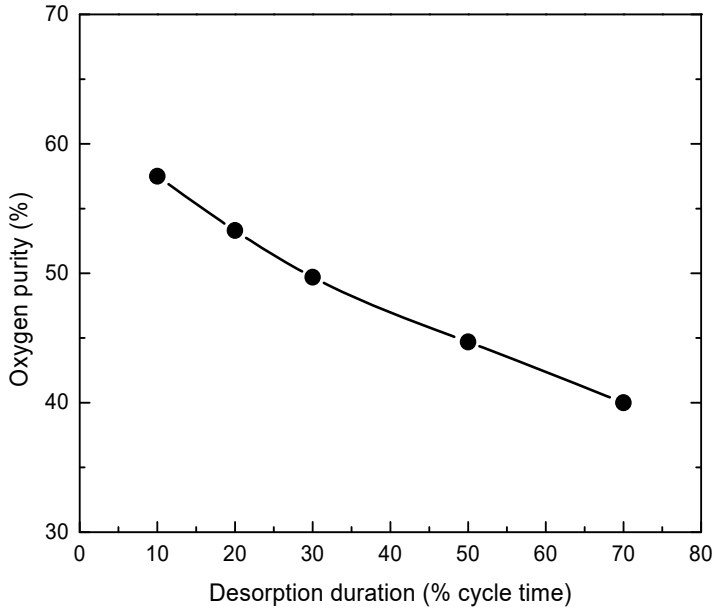

Figure 16. The effect of desorption duration on oxygen purity

The effect of flow rate of purge gas on oxygen purity was also studied over a range from 10^{-5} to 10^{-3} mol/min as shown in Figure 17. The other conditions were defined below: 60 seconds of adsorption and 60 seconds of desorption for each cycle, the pressure was 40 psia for air, 2 psia for purge gas. The flow rate of air was kept constant as 0.05 mol/min.

It was found that by reducing the flow rate of purge gas, the oxygen purity can be greatly increased. The oxygen purity reached 95% when the flow rate of purge gas was reduced to 10^{-5} mol/min. Because the only inpurity in the product was the purge gas, and the loss of recovered oxygen was much less than the loss of purge gas when reducing the flow rate of purge gas. For example, when the flow rate of purge gas was reduced from 0.001 to 0.0005 mol/min, there was only a 20% loss of the recovered oxygen. Therefore by reducing the flow rate of purge gas, the percentage of purge gas will be lowered.

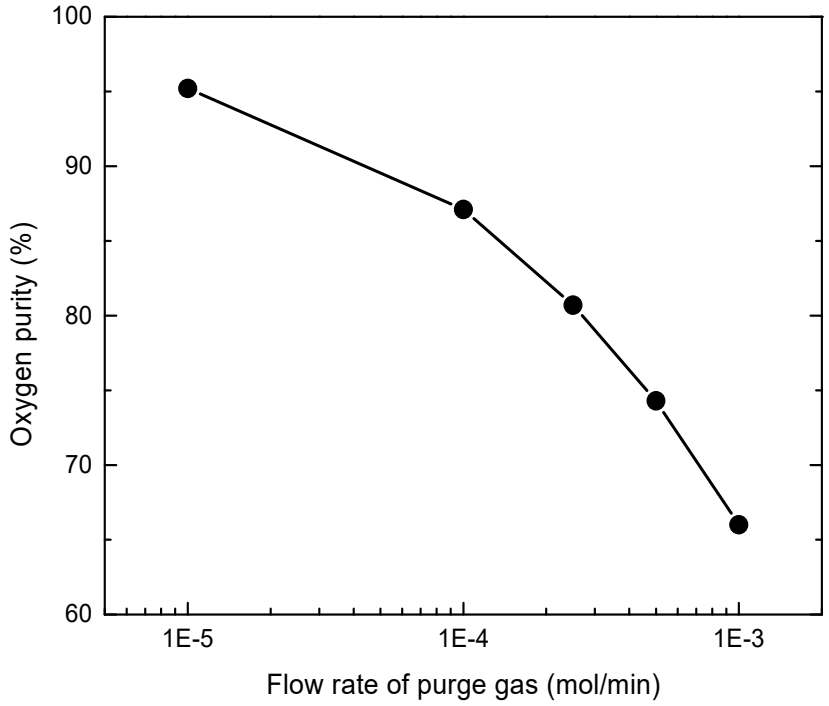

Figure 17. Effect of flow rate of purge gas on oxygen purity

As discussed above, adsorption pressure, desorption duration, and flow rate of purge gas has been considered as the main effects on oxygen purity for the product. But the most significant effect should be the flow rate of purge gas. it can be concluded that operating parameters of the PSA process with adsorption pressure of 40 psia, cycle time of 120 seconds (60 seconds of adsorption and 60 seconds of desorption), and purge flow rate of 10^{-5} mol/min yield optimal results. At the optimal condition, the oxygen purity reached 95%.

The oxygen concentration profile for the first cell of adsorption column for the first six cycles at the optimal conditions was plotted in Figure 18. For adsorption, the curve showed the oxygen profile at the inlet, it sharply increased to 0.21 at the beginning of adsorption for each cycle, which means breakthrough was rapidly achieved. For desorption, the curve showed the oxygen profile at the outlet. Oxygen fraction of the product gas was close to 1 at the beginning of desorption, and then decreased to 0.92 gradually. The average concentration of oxygen should be close to 95% as suggested before.

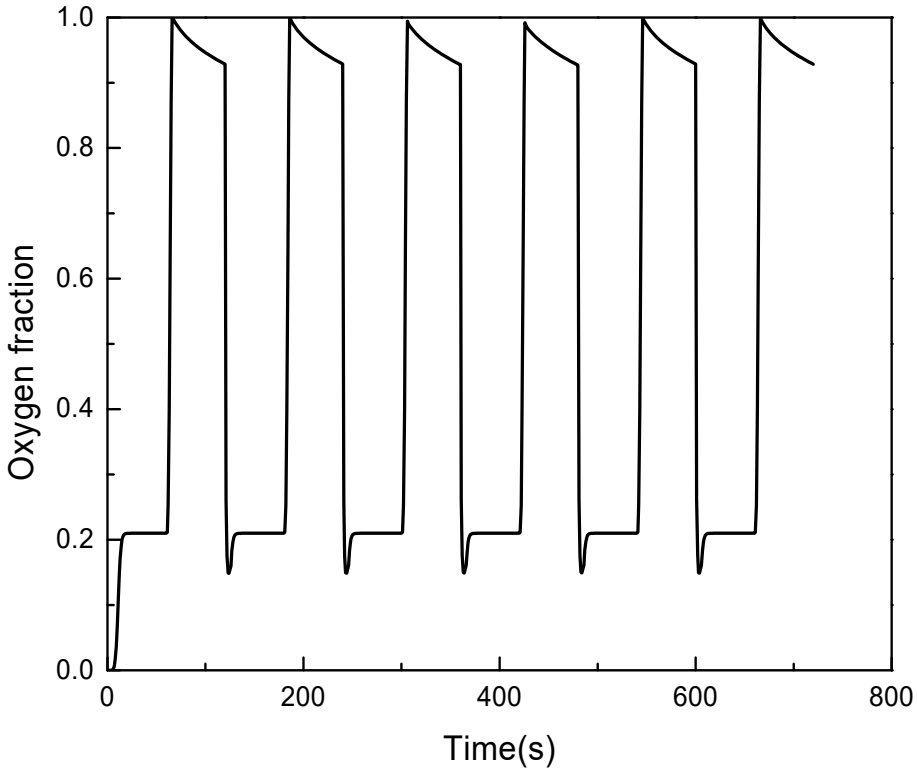

Figure 18. Oxygen profile for the first cell of adsorption bed

4. Conclusions

Perovskite-type oxide $La_{0.1}Sr_{0.9}Co_{0.9}Fe_{0.1}O_{3-\delta}$ (LSCF 1991) pellets were prepared by a pellet press. The crush strength and attrition resistance of the pellet samples sintered at different temperatures were tested. The result shows that pellets sintered at 1000 °C have the best mechanical strength.

A Matlab routine was developed to simulate adsorption and desorption process. The simulation result was proved to match the experimental data. The simulation result was also close to another professional adsorption simulation software, ProSim DAC. The simulation routine was further used to simulate and optimize a cyclic PSA process. Based on the study on the effect of process parameters, it is found that high adsorption pressure, low desorption duration and low

purge flow rate could yield high oxygen concentration in the product. At the optimal condition, with adsorption pressure of 40 psia, cycle time of 120 seconds (60 seconds for both adsorption and desorption), and purge flow rate of 10^{-5} mol/min, an oxygen purity of 95% was obtained.

Nomenclature

C_i: Partial concentration of i compound in the gas phase (mol/m^3)

q_i: Partial concentration of i compound in the adsorbed phase (mol/kg of adsorbent)

ε: Vacuum ratio of the adsorbent bed

ρ_p: Density of the adsorbent particle (kg/m^3)

D_L: Axial dispersion coefficient (m^2/s)

y_i: Mole fraction of component i

z: Column length (m)

u: Mixture effective speed (m/s)

t: Time (s)

K_{fi}: Mass transfer coefficient in the gas phase (m/s)

S_p: Specific surface per bed volume unit (m^2/m^3)

C_i^*: Gas phase particle concentration at the interface of I compound (mol/m^3)

ρ: gas phase density (kg/m^3)

u: gas phase superficial velocity (m/s)

d_p: Adsorbent particle radius (m)

μ: Gas phase dynamic viscosity (Pa*s)

D_{mi}: Molecular diffusion coefficient in gas phase (m^2/s)

K_{pi}: Mass transfer coefficient of i compound in the adsorbed phase

q_i^*: Partial concentration at the solid interface of i compound (mol/kg)

D_{si}: Surface diffusion coefficient (m^2/s)

E_{si}: Activation energy for the surface diffusion (J/mol)

τ_s: Surface tortuosity factor

q_{m0}, q_{m1}, K_0, K_1: Constants of Langmuir equation

P_0: Initial pressure (atm)

P_f: Feeding pressure (atm)

P_p: Purging pressure (atm)

m, c: Ergun equation coefficient

K: Bed permeability (cm^2)

References

[1] D. Acharya et al., "Development of a high temperature oxygen generation process and its application to combustion power plants with carbon dioxide capture," in Proceedings of the 22nd Annual International Pittsburgh Coal Conference, 2005.

[2] D. M. Ruthven and S. Farooq, "Air separation by pressure swing adsorption," Gas Separation & Purification, vol. 4, no. 3, pp. 141–148, Sep. 1990.

[3] M. M. Hassan, D. M. Ruthven, and N. S. Raghavan, "Air separation by pressure swing adsorption on a carbon molecular sieve," Chemical Engineering Science, vol. 41, no. 5, pp. 1333–1343, 1986.

[4] K. P. Kostroski and P. C. Wankat, "High recovery cycles for gas separations by pressure-swing Adsorption," Industrial & Engineering Chemistry Research, vol. 45, no. 24, pp. 8117–8133, Nov. 2006.

[5] Z. Yang, Y. S. Lin, and Y. Zeng, "High-temperature sorption process for air separation and oxygen removal," Industrial & Engineering Chemistry Research, vol. 41, no. 11, pp. 2775–2784, May 2002.

[6] Z. H. Yang and Y. S. Lin, "High-temperature oxygen sorption in a fixed bed packed with Perovskite-Type ceramic Sorbents," Industrial & Engineering Chemistry Research, vol. 42, no. 19, pp. 4376–4381, Sep. 2003.

[7] Q. Yin, J. Kniep, and Y. S. Lin, "Oxygen sorption and desorption properties of Sr–Co–Fe oxide,"Chemical Engineering Science, vol. 63, no. 8, pp. 2211–2218, Apr. 2008.

[8] Q. Yang, Y. Lin, and M. Bülow, "High temperature sorption separation of air for producing oxygen-enriched CO2 stream," AIChE Journal, vol. 52, no. 2, pp. 574–581, Jan. 2006.

[9] Z. Yang and Y. S. Lin, "Equilibrium of oxygen sorption on perovskite-type lanthanum cobaltite sorbent,"AIChE Journal, vol. 49, no. 3, pp. 793–798, Mar. 2003.

[10] R. S. Todd and P. A. Webley, "Mass-transfer models for rapid pressure swing adsorption simulation,"AIChE Journal, vol. 52, no. 9, pp. 3126–3145, Sep. 2006.

[11] M. A. Latifi, D. Salhi, and D. Tondeur, "Optimisation-based simulation of a pressure swing adsorption process," Adsorption, vol. 14, no. 4-5, pp. 567–573, May 2008.

[12] L. Jiang, L. T. Biegler, and V. G. Fox, "Simulation and optimization of pressure-swing adsorption systems for air separation," AIChE Journal, vol. 49, no. 5, pp. 1140–1157, May 2003.

[13] A. Beeyani, K. Singh, R. Vyas, and S. Kumar, "Parametric studies and simulation of PSA process for oxygen production from air," Polish Journal of Chemical Technology, vol. 12, no. 2, Jan. 2010.

[14] S. W. Chai, "Experimental simulation of rapid pressure swing adsorption for medical oxygen concentrator and numerical simulation of the critical desorption-by-purge step," Lehigh University, 2011.

[15] J. Hart, M. J. Battrum, and W. J. Thomas, "Axial pressure gradients during the pressurization and depressurization steps of a PSA gas separation cycle," Gas Separation & Purification, vol. 4, no. 2, pp. 97–102, Jun. 1990.

Appendix III
LP Amina Report

Dr. Mathew Targett

Final Report

"Sorbent-Based Oxygen Production for Energy Systems"
Federal Grant Number: DE-FE0024075

For Reporting Period of November 1, 2014 to September 30, 2016

Matthew Targett
LP Amina

LP Amina prepared an economic model for sorbent-based oxygen production based on the following: experimental thermodynamic data generated from TGA measurements of the new perovskites, kinetics data generated from bench scale testing of the new perovskites together with Aspen^{TM} process simulations and capital cost estimator. All were based on the following plant design and operational assumptions. All these assumptions were viewed a key input variables for the financial model and helped to guide cost optimization.

- Product Oxygen Purity, >98%
- Perovskite sorbent costs, $6,000/ton
- Two thermally integrated, close-coupled, equal size "reaction volumes" for sorption and desorption (Tube and shell reactor)
- Adsorber-Desorber Tubes, 100 mm dia. tubes
- 12 cycles per hour, 5 minute cycles
- Adsorption-Desorption Temperature: 550^{o}C
- Adsorption Pressure: 7 psig
- Desorption Pressure: -7 psig
- Sorbent Performance: 0.001 - 0.002 g O_2/g sorbent per cycle
- Sorbent Pellets: 5mm x 1mm dia. pellets
- Blower productivity @ 7psig discharge pressure: 14.4 KW-hr power consumption per ton air feed
- Oxygen yield as a percent of air fed to adsorber: 50%

Two commercial cases were considered: 1) a large-scale oxygen plant, e.g., to supply an oxy-combustion or IGCC power station, and 2) a smaller scale oxygen plant, e.g. for an electronics fab or a small-scale 5MW coal fed IGCC facility. We used the preferred, current lowest cost technologies for comparison at each scale: A cryogenic oxygenic air separation unit (ASU) for the large scale benchmark (400,000 Nm^3/hr oxygen) and a vacuum pressure swing adsorption (VPSA) system for the smaller scale benchmark (2,500 Nm^3/hr oxygen). Table 11 below summarizes the estimated capital and operating costs for sorbent-based oxygen delivery at 2,500 Nm^3 O_2 per hour (94 ton O_2 per day) and at 400,000 Nm^3 O_2 per hour (15,000 ton O_2 per day).

Table 1 contains the list of major equipment along with installation cost estimates. For OPEX, we considered only electric power, equipment maintenance, and the sorbent make-up costs. Labor and SG&A were not included because we presume that these would be similar to the legacy, benchmark technologies. These numbers were rolled into the cost of oxygen and summarized in Table 2 below. It must be further noted that in all the LCO cases presented it is additionally assumed that the adsorber-desorber heating needs

are essentially eliminated due to close coupling with high temperature IGCC and oxy-fired combustion processes.

Table 1. Capital Cost Estimates for Sorbent-based Oxygen Plant

	2,500 Nm3/hr O2 supply (small comm'l)		***400,000 Nm3/hr O2 supply (large comm'l)***	
	3.57 tonnes/hr		*572 tonne/hr*	
Equipment	Purchased Cost ($)	Installation Cost ($)	Purchased Cost ($)	Installation Cost ($)
Air blower	$32,400	$8,100	$5,184,000	$1,296,000
Adsorber/Desorber vessel	$940,000	$235,000	$58,311,000	$37,600,000
Sorbent	$1,506,000	$0	$240,960,000	$0
Vacuum Pump	$1,620	$405	$259,200	$64,800
Equipment Costs	**$2,480,020**	**$243,505**	**$304,714,200**	**$38,960,800**
Installed equipment cost	$2,723,525		$343,675,000	
+ Direct costs (Others)	$438,309		$28,689,390	
Total direct cost	**$3,161,834**		**$372,364,390**	
+ Indirect costs	$711,035		$46,540,566	
Fixed Capital Investment	**$3,872,869**		**$418,904,956**	

As a basis for comparison, we used publicly available information provided in reference 3. In general, we find that the LCO process has slightly higher capital cost than both the large ASU and the VPSA systems, but operational costs are lower. In order to make a cost of oxygen comparison, we assigned a capital cost of 8% per annum, and then divided by the tons of oxygen produced. As can be seen in Table 2 once we consider the cost of capital, the sorbent-based cost of oxygen is 26% lower than VPSA oxygen; and additionally the sorbent-based cost of oxygen is 13% lower than ASU oxygen. The source of the savings versus VPSA is in the fact that the desorber blower is about 1/5th the size of a VPSA resulting in substantial energy savings. Not surprisingly, the advantages of LCO are less than a large-scale ASU because LCO numbers up for achieving scale and similar to VPSA does not enjoy as high economies of scale as cryogenic ASU processes do. It is noteworthy that VPSA is much more expensive than ASU at large scales, and becomes non-competitive with ASU technology around 100 tonne/hr, whereas LCO is projected to be cost-competitive with ASU for large scale applications. This is due to its more efficient use of waste heat (in the context of an IGCC or oxy-combustion system) and lower electrical consumption.

Table 2. Comparison of oxygen production costs

Oxygen capacity (Nm3/hr)	***2,500***		***400,000***	
System type	VPSA	LCO	ASU	LCO
Specific power required kWhr/tonne O_2	255	144	223	144
CAPEX $mio	4.43	3.87	377	419
Annualized cost of capital $mio	0.354	0.310	30.2	33.5
Maintenance (3% of capital), $mio	0.133	0.116	11.310	12.567
Cost of capital $/tonne O_2	11.3	9.9	5.48	6.7
Maintenance costs, $/tonne	4.2	3.7	2.3	2.5
Sorbent make-up costs, $/tonne O_2	Included	0.51	0	0.51
Electricity cost, $/tonne O_2	17.9	10.6	15.6	10.6
Total cost of oxygen $/tonne O_2*	**33.4**	**24.7**	**23.3**	**20.3**
% savings v. benchmark	***N/A***	***26%***	***N/A***	***13%***

** Does not include SG&A, direct labor (which should be similar in benchmark and LCO cases)*